LUND UNIVERSITY

FACULTY OF SCIENCE

Beyond traditional tomography: X-ray multi-projection imaging for additive manufacturing

María Esther Vilar Álvarez

Thesis submitted for the degree of Bachelor of Science
Project duration: 2 months (15 ECTS)
Spring semester 2023

Supervisor: Dr. Pablo Villanueva Perez
Co-supervisors: Zisheng Yao and Yuhe Zhang

Department of Physics
Division of Synchrotron Radiation Research
Date of examination: 15-06-2023

ABSTRACT

The main aim of this bachelor thesis is to push the limits of 3D X-ray imaging by studying the minimum number of projections required to retrieve high-quality reconstructions for additive manufacturing processes. This project first focuses on understanding how X-ray tomography works, by reconstructing additive manufacturing data already obtained (from PSI, TOMCAT beamline) using two standard reconstruction algorithms, GRIDREC and SIRT. Once 3D reconstructions are obtained with state-of-the-art algorithms, a novel deep-learning algorithm that can reduce the constraints regarding the number of projections and the angular range was used, ONIX. From this, the results obtained by the state-of-the-art approaches and those novel ones in terms of the relevant imaging parameters are compared. This comparison also involves checking given settings where traditional reconstruction fails and analyzing the type of results that novel methods yield. After studying how ONIX can work with a low number of projections, an outlook is provided on how deep learning methods can be used in the future development of additive manufacturing, or 3D printing.

Acknowledgements

I wish to express my deep gratitude to my supervisor Pablo Villanueva Pérez, for all his valuable help, guidance, and support during the past months. Thank you for your unwavering dedication and infectious enthusiasm for the subject, which have been truly inspiring to me along this journey.

I am extremely grateful to my co-supervisors Zisheng Yao and Yuhe Zhang for their kindness, encouragement, and patience in answering all my questions, and all my numerous emails. Thank you, Pablo, Yuhe, and Zisheng as well for introducing me and helping me discover the fascinating field of deep learning.

My special thanks to Emanuel Larsson, Sam McDonald, and all the researchers I met at MAX IV and to the members of the Synchrotron Division at Lund University, especially Julia Rogalinski and Myrto Asimakopoulou, for their warm welcome, priceless help, and constant feedback. I have learned so much from all of you.

I cannot forget my secondary school physics teacher, Mr. John O'Sullivan, the first person who opened my eyes to the enthralling field of physics. I am forever grateful for everything you taught me, and for making me realize I could have a future in physics.

I could not have done this without my mother's ever-present and unconditional support in everything I do, throughout my whole life. Thank you so much for teaching me never to give up and never be afraid to follow my dreams, and for being the one to nurture my passion for learning and instill in me the joy of studying. I extend my heartfelt gratitude to my father, my sister, my grandparents, and my friends for their constant encouragement and love. And a special mention to my late grandfather Dr. Raúl Álvarez, for his example of perseverance, humility and solidarity.

CONTENTS

Abstract **II**

Acknowledgements **III**

Acronyms **V**

List of Figures **VI**

List of Tables **VI**

1 Introduction **1**

2 Theoretical Background **2**
2.1 The physics behind X-rays 2
2.1.1 Interactions of X-rays with matter. 2
2.1.2 Sources of X-rays. 5
2.2 Applications with X-rays 8
2.3 X-ray Tomography 8
2.3.1 A basic outline of tomography 8
2.3.2 Algorithms for tomographic reconstruction. 11
2.3.3 Limitations - traditional methods for reconstruction 13
2.4 Beyond Traditional Tomography 14
2.4.1 Quick overview of deep learning 14
2.4.2 ONIX - Optimized Neural Implicit X-ray imaging - from 3D to 4D 15

3 Method and Tools **19**
3.1 PART I - Traditional Tomographic Reconstructions 19
3.2 PART II - Reconstructions with ONIX 21

4 Results & Discussion **23**
4.1 PART I - SIRT vs GRIDREC 23
4.1.1 Studying the performance of state-of-the-art tomographic algorithms under the constraint of a limited number of projections . . 23
4.2 PART II - Image reconstruction with ONIX 26
4.2.1 Studying the performance of the XMPI deep learning algorithm, ONIX, with a limited number of projections, and comparing it with the results obtained for SIRT and Gridrec under the same constraint. 26

5 Outlook **30**
5.1 ONIX and Additive Manufacturing 30

6 Conclusion **30**

7 Appendix **35**

ACRONYMS

AM Additive Manufacturing

CNR Contrast-to-noise ratio

DL Deep Learning

FBP Filtered Backprojection

ONIX Optimized neural implicit X-ray imaging

RF Radio Frequency

SNR Signal-to-noise ratio

XMPI X-ray multi-projection imaging

XFELs X-ray free electron lasers

List of Figures

2.1 Refractive index decrement, absorption index and transmission 3
2.2 Mass attenuation coefficient 4
2.3 Development of the different X-ray sources now available from 1960 until 2020, characterized by their brightness [12] 5
2.4 X-ray tube 6
2.5 X-ray tube spectrum 6
2.6 Synchrotron facility 7
2.7 How X-ray tomography works 9
2.8 Example of a sinogram 10
2.9 Fourier Slice Theorem 11
2.10 Filtered Backprojection 12
2.11 Working principle of ONIX 16
3.1 ROIs for reconstructed slices 20
3.2 Filtered backprojection vs gridrec 21
3.3 Ground truth and coarse output 22
4.1 SIRT reconstruction: decreasing iterations 23
4.2 Denoised Gridrec reconstruction 24
4.3 Gridrec reconstruction: decreasing number of projections (I) 25
4.4 SIRT reconstruction: decreasing number of projections (I) 25
4.5 Coarse output figures and final 3D rendering for **Training Attempt 1** . . 27
4.6 Reconstructions with ONIX 28
4.7 Gridrec tomographic reconstructions for a decreasing number of projections. 28
4.8 SIRT tomographic reconstructions for a decreasing number of projections. 28
7.1 Coarse output figures for **Training Attempt 1** 35
7.2 Coarse output figures for **Training Attempt 2** 36
7.3 Coarse output figures for **Training Attempt 3** 36
7.4 Coarse output figures for **Training Attempt 4** 36

List of Tables

3.1 Known data from the synchrotron X-ray tomography beamtime at PSI . 19
3.2 ONIX parameters - Training Attempt 1 22
7.1 Training Attempt 1 35
7.2 Training Attempt 2 35
7.3 Training Attempt 3 35
7.4 Training Attempt 4 35

1 INTRODUCTION

Since the discovery of X-rays as a form of electromagnetic radiation in 1895 by Wilhelm Röntgen, they have been widely exploited in science. One of their most exploited properties is their penetrating power, which makes them a primordial tool in the non-destructive study of matter. X-rays can penetrate materials in a non-invasive manner, allowing the study of internal structures. The way X-rays interact with different structures is the basis by which a 3D study of these materials can be effectively made, as the energy and intensity of X-rays vary when it interacts with individual elements. This makes X-rays an important tool in 3D imaging. Two such examples and the focus of this thesis work, are X-ray tomography and XMPI (X-ray multi-projection imaging). Tomography is the state-of-the-art technique to explore matter in 3D with X-rays, executed by collecting a large number of X-ray projections while the sample is rotated, which are used to reconstruct 2D slices, and these are then stacked to yield the 3D visualization. XMPI is a technique used for the same purpose but which involves taking multiple X-ray images of a sample from various angles simultaneously. [1, 2].

To obtain the 3D tomographic reconstructions of samples studied, numerous algorithms are currently being used. However, these state-of-the-art algorithms have the shortfall of failing when their input data is limited. Recognizing this reality, the objective is to retrieve high-quality reconstructions from sparse projections. For this, a newly developed deep learning framework for XMPI, called ONIX is used, which proves capable of yielding 3D reconstructions when a low number of projections are used. The two state-of-the-art algorithms are studied by examining how they respond when the number of projections is gradually decreased, and comparisons are made with the result obtained with ONIX, as ONIX is made to work starting from the limit where it is evident that state-of-the-art algorithms have completely failed, namely below 10 projections.

The advent of new algorithms like ONIX, which works with reconstructions both in 3D and 4D (i.e. where the coordinate of time is also included) can have a meaningful and substantial impact in the field of additive manufacturing, where the study of 3D dynamics of the materials being manufactured is still in its early stages of development. This is because they cannot perform tomography as they cannot rotate the sample fast enough to collect 3D data. Thus, XMPI is required, which collects a few projections to study the dynamics of the materials. That is, a tool through which the morphology and the dynamics of a material can be studied in real-time, with the certainty of high spatial and temporal resolution of the sample being examined, and this can be achieved without an extensive amount of data which is both time-consuming and costly. 4D-ONIX can permit the close evaluation of the dynamic behavior of the manufacturing process, with the advantages of fast acquisition time and minimal input data needed.

2 THEORETICAL BACKGROUND

2.1 THE PHYSICS BEHIND X-RAYS

2.1.1 INTERACTIONS OF X-RAYS WITH MATTER.

Understanding how tomography can be achieved requires a knowledge of how exactly X-rays interact with matter, as imaging techniques work on this principle. X-rays are photons with energy characterized as $E = hc/\lambda$ where h is known as *Planck's constant*, an experimentally observed constant value of 6.62607015 x 10^{-34} m^2 kg/s [3], c is the speed of light in vacuum and λ is the wavelength. In the electromagnetic spectrum, X-rays are shown to have energies approximately between 100 eV and around 100 keV, [4]. X-rays obey the wave-particle duality, and this explains phenomena such as diffraction or refraction, and the interactions of X-rays with matter. Taking X-rays as waves, they can be mathematically described by the following equation:

$$\mathbf{E}(\mathbf{r}, t) = \mathrm{Re}\{\mathbf{E}(\mathbf{r})e^{-iwt}\} \tag{2.1}$$

where the complex field amplitude $\mathbf{E}(\mathbf{r})$ is expressed as:

$$\mathbf{E}(\mathbf{r}) = \mathbf{E_0}e^{\pm i\mathbf{k}\cdot\mathbf{r}} \tag{2.2}$$

where $\mathbf{E_0}$ represents the amplitude of the electromagnetic wave. To simplify calculations, we can take a monochromatic wave traveling in the positive z-direction. Monochromatic waves are characterized by having a single frequency/wavelength that does not change over time. It can then be expressed as a time-independent wave equation, and we would have:

$$E_{in}(z) = E_0 e^{ik_z z} \tag{2.3}$$

In this case, the wave vector $\mathbf{k}$ in Equation 2.2 is now the wave number, given as $k = 2\pi/\lambda$. If we take a sample positioned between $z = 0$ and $z = z_0$, a line integral describes the total interaction of the X-ray wave as it travels through the chosen medium:

$$E_{out} = E_{in} \exp\left(ik \int_0^{z_0} n(z)dz\right) \tag{2.4}$$

In this equation, we are referring to both the incoming and outgoing X-ray waves, and $n(z)$ is the spatial distribution, provided by the formula of n, the coefficient of refraction:

$$n = 1 - \delta + i\beta \tag{2.5}$$

This coefficient encompasses information about the attenuation properties of the X-rays (β) as well as the phase-shifting properties (δ), also called the refractive index decrement. Equation 2.4 is a direct result of the *projection approximation*. This approximation is used in the field of X-ray imaging, to simplify the study of the wave equation. The projection approximation works by assuming that the rays entering a volume are not affected by scattering or diffraction. This implies that the waves simply propagate through a medium that has a given index of refraction n, which can vary along the direction of the propagation of the light wave. The index of refraction contains information about the medium and executing an integration accounting for the cumulative effects such medium has on the transmitted ray. For X-rays, due to their high energy and their associated weak interactions with matter, n is close to unity and the values

of δ and β are small. [5] By making a substitution of this formula into Equation 2.4 we obtain:

$$E_{out} = E_{in} \exp(ikz_0) \exp\left(-ik \int_0^{z_0} \delta(z)dz\right) \exp\left(-k \int_0^{z_0} \beta(z)dz\right) \tag{2.6}$$

From here, the phase difference between propagating waves ϕ is denoted as:

$$\phi = \arg(E_{out}) - \arg(E_{in}e^{ikz_0}) = -k \int_0^{z_0} \delta(z)dz \tag{2.7}$$

Likewise, the attenuation is written as:

$$A = 1 - T = 1 - \left(\frac{|E_{out}|}{|E_{in}e^{ikz_0}|}\right)^2 = 1 - \exp\left(-2k \int_0^{z_0} \beta(z)dz\right) \tag{2.8}$$

where T stands for the transmission of the X-rays. When carrying out the X-ray imaging, a *flat-field image* has to be acquired, which refers to the propagation of the incoming field, through the sample space when the sample was not there. Both *delta* and *beta* are dependent upon the photon energy. Figure 2.1 shows this energy dependence of the coefficients of the complex refractive index.

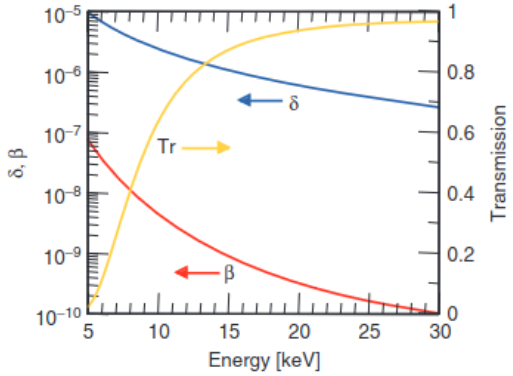

Figure 2.1: Plot for the refractive index decrement *delta*, the absorption index *beta*, and the transmission as a function of energy (of range between 5 and 30 keV) for a 1mm sample of flesh $C_{12}H_{60}0_{25}N_5O_{25}$. [6]

Figure 2.1 shows how with increasing energy, the transmission of the photon likewise increases, and the attenuation coefficient decreases with a sharper peak with higher energies than does the refractive index decrement. This can be seen also from Eq.2.8, more energy can be transmitted through the medium if there is a decrease in β, giving higher transmission.

The index of refraction equation (Eq. 2.5) is a formalism that explains how an X-ray will behave as it propagates through a medium, which is then required to understand the actual physical processes involved in the interactions of X-rays in matter. There are three main important mechanisms, namely, the *photoelectric effect*, *Compton scattering*, and *Rayleigh scattering*. A quick description of each of these three mechanisms is provided below as to how they compare in terms of energy.

First, we discuss the photoelectric effect. When an X-ray interacts with a tightly bound electron within an atom, the photon gets absorbed and transfers its energy to

the photo-electron, ejecting it from the atom, and simultaneously causing the ionization of the atom. As a result of this process, electrons from the outer shells might fall into the vacant hole left by the ejected photo-electron. Two things can happen when the electron falls from the inner to the outer shells, 1) fluorescence, as a photon equal to the loss in energy will be emitted, or 2) this energy can, in turn, contribute to eject yet another electron from the atom, known as the Auger electron. The photoelectric effect depends on the atomic structure and is perhaps the most crucial contributor to the attenuation of the X-rays, which describes the reduction of the intensity of an X-ray as it travels through matter. [7, 8]

Secondly, there is Compton scattering or inelastic scattering. It occurs when the incoming photon interacts with an electron from the outer orbit of the nucleus, that has low binding energy. Its path gets deflected as a result of this encounter and is therefore scattered in a different direction. A percentage of the photon's energy is transmitted to the electron, causing it to recoil and be ejected from its shell, which once again ionizes the atom. Its cross-section is heavily dependent on the electron density of the material. At higher energies, Compton scattering becomes the main contribution to the X-ray attenuation. [9, 8]

Finally, we are left with Rayleigh scattering or elastic scattering. As the name implies, the incoming and outgoing photons have the same energy, implying that even after scattering, there is no loss in their energy. It principally contributes to the phase shift of X-rays and has no effect in attenuating the X-rays at very high energies, as it only happens for lower energy values. In the same way as inelastic scattering, its cross-section also depends on the electron density of the material, and on the individual properties of both the photon and the electron, such as photon energy.

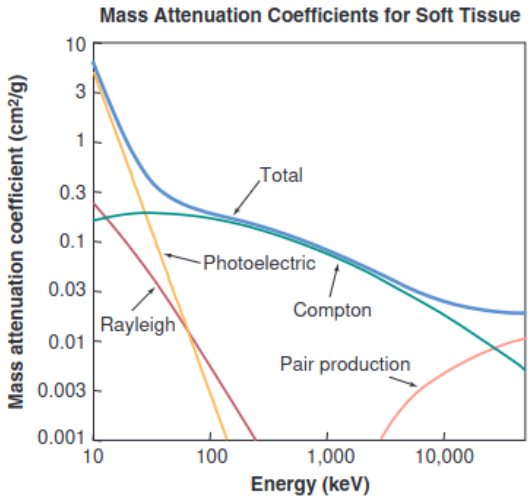

Figure 2.2: Mass attenuation coefficient as a function of energy for soft tissue (Z = 7) [10]

Fig. 2.2 shows the three main processes through which X-rays interact with matter and their contributions to the respective mass attenuation coefficients with respect to energy. Pair production is also included in the figure, but this is not relevant to the study of X-rays. For energy ranges between 10 to 200 keV (The X-ray energy regime), one only has to worry about the photoelectric effect and Compton and Rayleigh scat-

tering. At low energies, approximately between 10 - 100 keV, the photoelectric effect is the most dominant process. After this threshold, it starts to rapidly decrease, and at any higher energies, the photoelectric effect is not significant at all. Compton scattering, within that same energy range, shows a more leveled plateau, and its decrease is steady and slow with increasing photon energy. Rayleigh scattering is the less dominant of the three interactions, and it is portrayed as a sharp decreasing linear curve, with a cross-section that decreases slower than the photoelectric effect. Rayleigh scattering takes place at low energies, of around 10 keV, After that, any increase in photon energy will lead to the probability of this interaction declining.

The characteristics of X-rays, such as their energies and thus the way they will interact with matter are highly determined by the X-ray source employed. That is why it is important to understand exactly how and where X-rays are produced, as this will in turn determine how X-rays can then be used.

2.1.2 Sources of X-rays.

X-rays can be obtained both through natural phenomena as well as through man-made mechanisms. The two main natural sources come from cosmic rays and from radioactive elements found on Earth. However, man-made X-ray radiation is the one commonly used in industry and research. Parameters such as brightness can be used to understand the properties of an X-ray source. The brightness of an X-ray beam can be used to establish the performance of an X-ray source and how the produced X-rays can be subsequently applied [11].

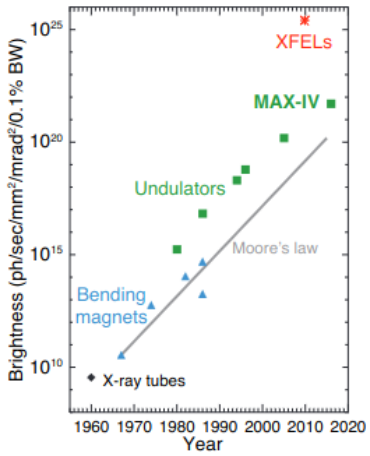

Figure 2.3: Development of the different X-ray sources now available from 1960 until 2020, characterized by their brightness [12]

Brightness refers to the amount of radiation that is either emitted by the source per unit area, per unit solid angle and per unit time. With this classification, it is possible to make comparisons between the different sources. Higher brightness typically means higher photon flux, which is required to obtain high-quality images with sufficient signal intensity, as the signal intensity will increase with an increase in the flux input to the detector.[13]. This increased signal strength is crucial to better discriminate between features in a reconstructed image, boosting the contrast and resolution.

Therefore, below, an outline of 3 important sources of X-rays will be given. In Fig 2.3, we can see a plot of the brightness as a function of the available x-ray sources throughout the decades.

Laboratory sources of X-rays refer to the X-ray tube, as shown in Fig. 2.4 below. Electrons are produced and emitted by a glowing filament (the cathode) and accelerated to energies within the keV range, towards the anode. The impact when the electrons hit the metal target causes the deceleration of the electrons, and their high kinetic energy is thus converted into X-rays.

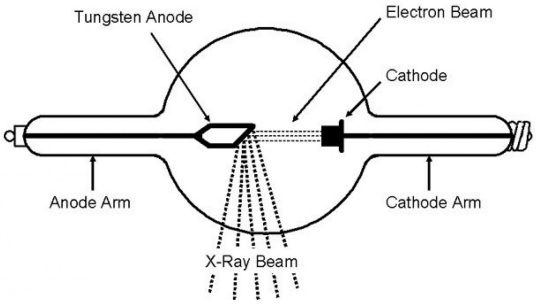

Figure 2.4: A general overview of how an X-ray tube works. Electrons are produced in the cathode when it is heated and these electrons are then accelerated towards the anode. When they strike this tungsten target, an X-ray beam is produced. [14]

The release of X-rays happens in two distinctive ways, (i) through a continuous spectrum, referred to as the *bremsstrahlung* radiation, which can only attain energies as high as the voltage value applied to the tube and then (ii) a discrete line spectrum, caused by fluorescent radiation. The difference in energy produces a characteristic X-ray. Both spectra are superimposed and certain techniques are required to isolate either of the two. The spectra obtained from an X-ray tube is presented in Fig. 2.5.

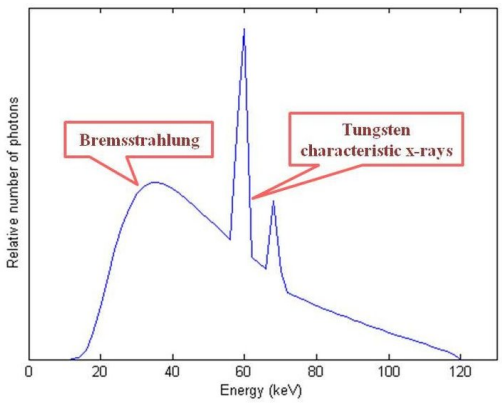

Figure 2.5: X-ray spectra obtained from an X-ray tube, showing both the bremsstrahlung radiation as well as the two peaks of the discrete (or characteristic) line spectrum of the Tungsten X-rays. The relative number of photos is analyzed as a function of the energy in keV. [15]

One of the challenges faced with the first X-ray tubes was the fact that when the high-energy electrons hit the anode, all their energy is transferred to the target material, which can cause damage to it due to overheating. To prevent this problem from happening, which is a limiting factor to the tube's power output, the rotating anode

was implemented and is now a necessary component found in modern X-ray tubes. The setup now includes an anode that is responsible for dissipating heat by way of fast rotations.

Two of the main drawbacks of using these sources is the fact that the wavelength is not tunable but dependent on the anode target material and they also have a relatively lower intensity as compared to the synchrotron radiation X-rays.

Synchrotron radiation is a form of electromagnetic energy occurring when particles (i.e. electrons) are accelerated to quasi-relativistic speeds, as they have their trajectories altered by magnetic fields. Synchrotron-radiation facilities have been specifically built around the world for the purpose of producing synchrotron radiation, which has been proven to be a brighter source of X-rays than then traditional laboratory X-ray sources. These X-rays are now widely used, for example, for the study of microscopic and submicroscopic samples, which require high photon flux and brightness. The design of a synchrotron facility is exhibited in Fig. 2.6. The two most important devices are the booster ring and the storage ring. The booster ring increases the energy of particles, which are then injected into the main storage ring, where they are accelerated in a circular motion, with the aid of the magnets used for constraining the particles in their orbit, and their energies are further increased, but this time over a much greater distance. These particles gain energy every time they pass through the RF (radio-frequency cavities). The storage ring is also given its name because it is intended to store the energy of the particles for extended periods of time. The optics and experimental hutches are where experiments with synchrotron radiation can take place, and the synchrotron radiation manipulated to suit the requirements of the experiment.

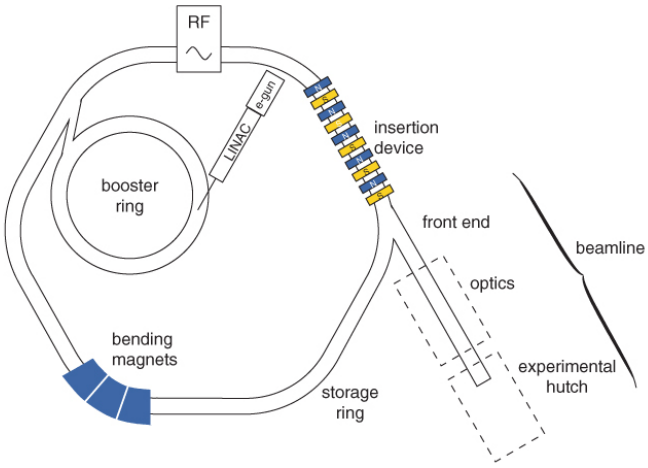

Figure 2.6: Synchrotron facility with all the necessary components for the generation of synchrotron radiation, where one can see the electron gun, LINAC, the booster ring, the storage ring, the RF cavity, the insertion device , the bending magnets and the respective beamline that contains the optics and experimental hutches.[16]

One such synchrotron facility is MAXIV, found in Lund, which has a storage ring of 3 GeV. As seen from Fig 2.3, MAXIV, as a fourth-generation synchrotron facility has achieved very high levels of X-ray brightness. For the production of this type of radiation, undulators are commonly used. These also provide higher photon flux and consist of dipole magnets that are periodically arranged. They generate alternating and static magnetic fields which trigger a deflection of the electrons. The N magnets placed end up acting as a diffraction grating, where constructive and destructive

interference periodically ensue. The wavelength λ depends on the magnetic field, implying that the radiation can be adjusted. In a similar fashion, the wave can become monochromatic, which can then be focused on the sample.

There exists a direct relationship between the intensity and the frequency of the emitted radiation and the strength of the magnetic field $\overrightarrow{B}$ and the energy of the accelerated particles. This leads to a clear and important advantage of synchrotron X-rays. They can be manipulated to achieve the desired results, such as a high spatial resolution.

A quick comment can also be made about XFELs (X-ray free-electron lasers), which as Fig.2.3 displays, are the sources that provide the X-rays with the greatest brightness, surpassing even the synchrotron sources. XFELs work on a similar principle as the synchrotron, with respect to high-energy electrons being accelerated to speeds approaching the speed of light. These electrons are then passed onto an undulator, and as they oscillate, intense bursts of X-rays are emitted. These signals then undergo a process of amplification, which increases their intensity. The resulting beam will be of high brightness. However, while providing these benefits of increased brightness and even faster processing times, XFELs are costly and require a large infrastructure to function, so they are mostly only used for specific and special research experiments, such as the study of ultrafast dynamics.[17]

For the purpose of this thesis project, the synchrotron-radiation facility is the desirable source of X-rays with the preferred brightness for the generation of high-quality images to achieve the goals outlined in Section 1.

2.2 Applications with X-rays

X-rays are, nowadays, at the forefront of scientific and industrial research.

One of the most important applications of X-rays lies within the field of medicine. The penetrative power of X-rays and the way they interact with matter serves as a tool through which the internal structure of the body can be examined. This is then applied for diagnostic purposes, such as the detection of abnormalities, like tumors, in the human body, as well as for general screening purposes. Furthermore, X-rays are also employed for cancer therapy, as hard X-rays, X-rays with a higher frequency and shorter wavelength and thus stronger penetrating ability, have shown to be effective in destroying malignant cells. [18]

X-rays are also greatly valued in other and varied fields, as we find X-rays in the analysis of microscopic biological samples. X-rays in the industry sector are needed in order to detect any flaws within materials (where industrial radiography would be used), as well as the study of materials like rubber, or plastic fibers. They are likewise found in the security sectors, such as airports, where X-ray screening tests are useful in the detection of any foreign objects.

2.3 X-ray Tomography

2.3.1 A basic outline of tomography

Having dealt with the physics and applications of X-rays in the previous sections, Section 2.3 will now incorporate the definitive application of X-rays in this bachelor's thesis: X-ray tomography, which integrates the learned concepts of X-ray attenuation

and X-ray brightness to effectuate tomographic reconstructions with the desired spatial and temporal resolutions. The technique through which the acquisition of slices is achieved as well as the reconstruction processes/algorithms involved in retrieving the final 3D reconstructions will be examined.

Tomography works on the principle of the detection of the attenuation of the X-ray beam through the sample. Images are acquired from a variety of angular positions, as the sample is rotated through a given angular range. The resulting projections allow for a 2D representation of the object (sinogram/radiograph), which is then further processed to achieve 2D reconstructions known as slices. When these slices are stacked together, the final 3D reconstruction of the sample is generated. This process is outlined in 2.7.

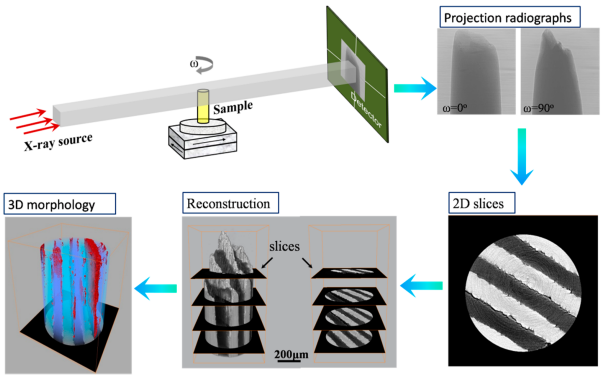

Figure 2.7: Outline of how synchrotron X-ray tomography works, from the acquisition process to the final 3D reconstruction. [19]

The sample rotates and the fixed X-ray beam generated by the synchrotron source passes through the sample. The transmitted photons are detected by a detector, which is responsible for converting it to visible light, that is, into a light pulse. The captured image is converted into discrete image elements or pixels. The intensity of the electric charge of a said pixel corresponds to the intensity of light that was captured. A pixel row is then simply a slice of the sample. The rotation of the stage where the sample is found occurs at an angle range of 0°- 180°, which still allows for the collection of all the necessary information, as the final range of 180°- 360 °is technically the same as before, and it is not required in order to acquire a complete reconstruction. The projections of the sample constitute line integrals. When a large number of projections at different angles has been obtained, the 2D resulting figure is known as a sinogram (Fig 2.8.) A sinogram shows the detected intensities for all pixels and detector positions for each slice for their corresponding rotation angles and carries information about the projections. Its two axes are the *angular axis*, which is a representation of the different projection angles at which the X-ray images of the object were acquired, and the *radial axis*, which depict the distance of the X-ray measurements from the central axis of rotation. With the sinogram, it is then possible to produce images of one slice. A sinogram gets its name from the fact that as the sample is rotated, a sinusoidal curve is shaped out.

To establish the number of projections N_θ and the rotation step $\Delta\theta$ that must be used, Crowther's criterion needs to be implemented. It helps resolve the angular separation between two projections that will reduce and prevent artifacts as well as provide all the necessary information required for the 2D and 3D reconstructions. Ba-

sically, Crowther's criterion is for sampling to the desired and uniform resolution, to achieve high-quality images with decreased noise. For example, in the case that we had a large sample, the number of rotation steps must be smaller, to improve the angular sampling. In this event, more projections are required to cover the rotation and obtain complete information from the sample while diminishing the artifacts in the reconstructed image. Crowther's criterion for an angle range of 180°degrees is shown in the equation below [12]:

$$N_\theta = \frac{\pi}{2} N_{x'} \tag{2.9}$$

where $N_{x'}$ is the number of pixels on each slice.

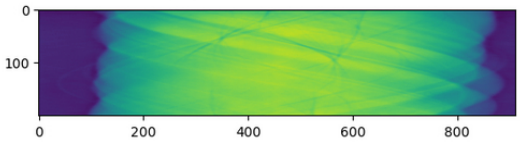

Figure 2.8: A sinogram of the X-ray projections. The sinogram contains information about the internal structure of the sample.

The mathematical representation of the sinogram is known as the Radon transform. It is given by the equation:

$$p(x')_{z,\theta} = \int_{-\infty}^{\infty} \int_{-\infty}^{\infty} f(x,y,z)\delta(x\cos\theta - y\sin\theta - x')dxdy \tag{2.10}$$

This is the Radon transform of the function $f(x,y)_z$, the 2D object slice, a function of both the position and the angle of rotation. High X-ray absorption is marked by a large value of $p(x')_{z,\theta}$. The goal of tomographic reconstruction is then to combine all the reconstructed slices to produce the 3D impression of the object, that is, finding the function $f(x,y)_z$ from the Radon transform function.

Finally, part of the process of 3D reconstruction involves the *Fourier-Slice Theorem*. The Fourier-Slice Theorem is a mathematical tool under which tomographic reconstructions work and serves as a strategy to obtain $f(x,y)_z$ from the Radon transform outlined above. A 2D function, once again given as $f(x,y)$, corresponding to a slice of the sample, has a Fourier transform $F(q_x,q_y)$

$$F(q_x,q_y) = \int\int f(x,y)e^{(q_x x + q_y y)}dydx \tag{2.11}$$

Characterizing $q_y = 0$, and thus considering one slice generates:

$$F(q_x,q_y=0) = \int \left[\int f(x,y)dy\right] e^{q_x x}dx \tag{2.12}$$

The equation in brackets is defined as $p(x)$, which correspondingly has a Fourier transform equation $P(q_x)$

$$P(q_x) = \int p(x)e^{iq_x x}dx \tag{2.13}$$

In this case, $p(x)$ is the integrated function of $f(x,y)$ along the y direction, which depends only on the variable x (one parameter). These equations can then be summarized in the following equality:

$$F(q_x,q_y=0) = \int p(x)e^{iq_x x}dx = P(q_x) \tag{2.14}$$

In other words, the Fourier Slice theorem states how the Fourier transform of a projection along a line described by a 2D function $f(x, y)$ is equal to one slice through its Fourier transforms in the direction of propagation. [1] This demonstrates that information about the slice of the 3D Fourier Transform of the original sample is contained in the 2D Fourier transform of a projection along a certain direction. Consequently, the Fourier Slice Theorem is a tool that makes possible the reconstruction of a 3D image from the corresponding 2D projections. A visualization of this theorem is illustrated in Fig. 2.9.

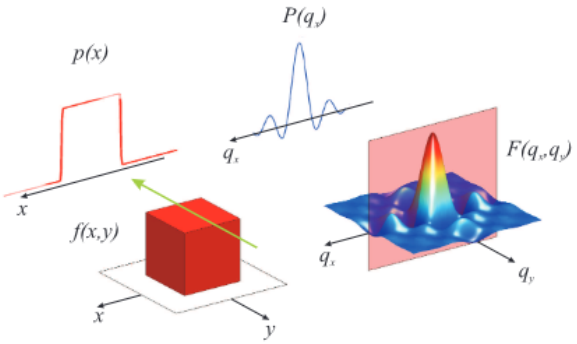

Figure 2.9: Image representation of the Fourier Slice Theorem. The $f(x, y)$ function is as 2D top hat function, with its corresponding Fourier transform $F(q_x, q_y)$. The projection of $f(x, y)$ along the y-axis yields a 1D top hat function $p(x)$, which is solely a function of x. The FT of of $p(x)$, $P(q_x)$ is equivalent to one slice of $F(q_x, q_y)$ when we set $q_y = 0$. [1]

2.3.2 Algorithms for tomographic reconstruction.

Filtered Back Projection

Filtered Back projection (FBP) is a commonly used algorithm for tomographic reconstruction. It is executed by combining the two methods of backprojection and filtering. In the case of backprojection, the collected projections are "backprojected" onto a two-dimensional image plane. Having, at first, a blank image, for each projection acquired, the X-rays are traced back through the object. This permits the calculation of the X-ray intensity at specific locations within the object, which are then assigned to the corresponding pixels in the image being reconstructed. This process is repeated until the image is gradually built up. This image is the cumulative contribution of X-rays from all angles. On its own, backprojection is not feasibly used as it yields highly blurry reconstructed images. Instead, to correct this, the filtering component is added. Fig. 2.10 demonstrates the need for this necessary step which will then yield a superior result of higher quality.

Filtering basically describes the process whereby low frequencies are attenuated in the projections. The Fourier Slice Theorem implies that areas of high frequency contain more detailed information while at low frequencies more blurriness is witnessed as a result of an overlapping of information. [20]. In order to correct for these variations in the frequencies, a radially dependent filter is applied, and this is done before the step of recovering $f(x, y)$ by doing the inverse Fourier transform.

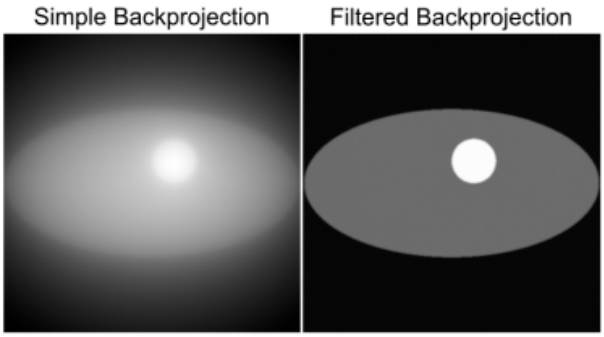

Figure 2.10: A representation of both backprojection and the improved filtered backprojection, in an attempt to highlight why filtering is a necessary step in the reconstruction technique. [21]

Another important step is the remapping of the data, taking into consideration that a pixel in the Fourier space represents a contribution to all pixels in real space. Therefore, the regridding involves changing from the Fourier space to the spatial domain in real space, polar to Cartesian coordinates. This is accomplished with a convolution kernel $\mathcal{W}(x, y)$, with the properties of being nearly symmetric in 2D and a separable function. This kernel provides a data sampling on the Cartesian coordinate grid and its effect can be easily removed afterward by a division between the object slice and the kernel itself. The *gridrec* algorithm is the result of the combination between filtered back projection and the Fourier space regridding. [12] Gridrec is one of the most used algorithms for tomographic reconstruction, due to its faster computational time and generates high-quality reconstructions. However, for this to occur it is important that Crowther's criterion is met, as using fewer projections will mean that the reconstructions will fall back to the low-quality range. This is exactly what can be observed in Fig. 4.4 of Subsection 4.1, as the number of projections is gradually decreased.

Iterative Reconstructions - SIRT (*Simultaneous Iterative Reconstruction Technique)*

An improvement in the processing algorithm of gridrec is found through the iterative algebraic methods. These reconstruction techniques are superior for a number of different reasons. Prior knowledge and constraints can be implemented into the algorithm, which entails that iterative algorithms will be able to handle the reconstruction better even if the input data is reduced. [22] This reduces the noise and the artifacts of the final 3D images. Moreover, the iterative procedure accounts for the discrepancy between the measured data and the predicted data produced by the present estimate. When this is taken into consideration, the resultant image quality is enhanced, with a higher likelihood of accurately resembling the target sample.

The main aim is to be able, through iterative processes, to improve the detail characteristics of the reconstructed image and reduce noise. To understand these algorithms, linear algebra concepts need to be drawn. The tomographic process can be described as a system of linear equations

$$\mathbf{A}\mathbf{x} = \mathbf{b} \tag{2.15}$$

where **A** stands for the forward projection matrix. It is a matrix of the form $m \times n$, where the rows m represent the projection angle and the columns n the output pixels of the reconstructed image. Then, **x** is the unknown value which has to be found, thus

the reconstructed object itself, which appears as a vector in the image space. And then **b** is the sinogram. The solution to this linear equation is solved by minimizing the norm $||\mathbf{A}\mathbf{x} - \mathbf{b}||$. And **x** is approximated with the equation:

$$\boldsymbol{x}^{k+1} = \boldsymbol{x}^k + \lambda_k \frac{\boldsymbol{b}_i - \langle \boldsymbol{a}_i, \boldsymbol{x}^k \rangle}{\|\boldsymbol{a}_i\|^2} \boldsymbol{a}_i^\top \tag{2.16}$$

where $\boldsymbol{a}_i$ is the i-th component of the matrix **A**, $\boldsymbol{a}_i^\top$ represents element i of the transpose matrix of **A**. The number of iterations written into the algorithm is given by k. Ultimately, the index i is equal to $i = k \bmod m + 1$, where m, as we have seen before, stands for the rows in matrix **A**. [23]

The iterative approach used in this thesis is the SIRT algorithm. Without delving any further into too mathematical detail, it can be briefly summarised as follows. The algorithm begins with an initial guess, which is an approximation of the object to be reconstructed. From this estimate, the algorithm calculates the projection error, which is the difference between the projection data and the data obtained from the initial estimate. Then the correction factor is calculated, which takes into account the contribution of each voxel (3D pixel) of the object to every projection. This factor is dependent upon the geometry of the sample and the projection matrix **A**. This is carried out by back-projecting the projection error. The algorithm then adds these two factors, the projection and correction factors, as a weighted sum to the original object estimate. Another factor, called the relaxation factor, is often multiplied as well as this stage. Small values of the relaxation factor increase the accuracy of the results, even if the convergence becomes slower. These steps are repeated in an iterative manner until a stopping point is reached, which can either be the number of iterations chosen for the algorithm to process or convergence being achieved. [24, 25]

2.3.3 Limitations - traditional methods for reconstruction

However, employing these two algorithms, Gridrec and SIRT, also comes with severe limitations, which can render a final product with a decreased resolution, and blurriness. A few of these limitations are discussed below:

- **Slow processing time** While algorithms like Gridrec can be generally considered to be one of the fastest state-of-the-art algorithms, making it a common choice for tomographic reconstruction, this is not the case for algebraic methods such as SIRT. These are mainly based on executing a large number of iterations, as a set of linear equations needs to be solved to yield a reconstructed image, resulting in a large matrix. All these multiple cycles of data processing cause an upsurge of the computational time required, as achieving iterative convergence can involve a large number of iterations. If a lot of data is required for the reconstruction, this will further slow down the algorithmic procedure. [26] So, even when iterative algorithms such as SIRT cause image noise to be radically decreased and image quality to increase it can nevertheless be a time-consuming process.

- **Ring artifacts** Ring artifacts appear as dark concentric rings centered around the rotation axis in the final reconstruction. They are usually the result of imperfect detector pixel elements, causing intensity variations. The irregularities in

the acquisition can result in important structural details being obscured or overlooked. However, to remove ring artifacts, and be able to normalize the variation of the detector, data undergo what is referred to as *flat-field correction*. Flat field correction involves the retrieval of dark fields (projection images taken without the sample and without the X-ray beam turned on) and flat fields (the same as for dark fields but this time with the X-ray beam on). Then normalization is achieved by also using the projection images obtained with the sample in place. The following formula describes this process:

$$N = \frac{\text{Projection image}(P) - \text{Dark field}(D)}{\text{Flat-field}(F) - \text{Dark field}(D)} \tag{2.17}$$

Applying flat field correction is likewise important for better image quality.

- **Limited capability when handling a limited amount of data** For algorithms such as FBP, the assumption is made that measurements are to be collected from a full range of views of a sample. In this case, a generous amount of input data is necessary for a better reconstruction. A decrease in the number of projections will thus cause a decrease in the resolution of the image [27]. Therefore, if a limited amount of data is available for analysis, the traditional algorithms will start to fail beyond a standard range.

2.4 Beyond Traditional Tomography

XMPI, Deep Learning & ONIX

From all the limitations specified in the preceding section, it is the last one we are concerned with. The aim is to retrieve high-quality tomographic reconstructions from a limited number of X-ray projections. A more advanced technique, XMPI (X-ray Multiprojection Imaging), is used. XMPI produces 3D structural information through the acquisition of multiple 2D projections taken at different tomographic angles simultaneously from the same sample. It works by illuminating the sample from those different angles at the same time. Therefore, each beam thus retains its corresponding projection information. [28]. As opposed to tomography, here there is no rotation of the sample. Powerful reconstruction algorithms for XMPI involve deep learning. One of the main advantages of deep learning is their ability to make a thorough analysis of input data, however limited it may be, and extract features of an object.

2.4.1 Quick overview of deep learning

Deep learning is a subset of machine learning and artificial intelligence (AI). It uses artificial neural networks, which are then trained to learn from the input data. Neural networks are formed by a group of interconnected neurons. Neurons are arranged in layers, which are categorized as follows, input layer(s), hidden layers, and output layer(s). Within these layers, the neurons are presented with specific functions, and they are in charge of manipulating the data received before transferring the output to other neurons. The representations that the network will use to make its predictions are included in the hidden layers. The network's ability to effectively process data and learn intricate patterns is largely dependent on how these layers are structured; such as their number and size. Forward and backward propagation describe processes that

aid to establish a higher degree of accuracy in the algorithms and when combined allow for the correction of errors. The layers that are placed together, act in a step-wise manner, improving the prediction by building upon the layer before it. This progression is *forward propagation*. On the other hand, *backward propagation* is an important phase in the training of the neural network, as it calculates for errors and adjusts any biases in the function by moving backward through the layers.

There are two main types of learning those deep learning algorithms are suited to learn. These are supervised and unsupervised learning. The main difference between these two types of learning lies in how the datasets are handled. Supervised learning works with labeled data, which with the aid of human intervention allows the model to progressively learn over time. The datasets are responsible for performing the role of "supervising" the algorithms, in order to obtain the desired outcomes and predictions. Supervised learning works with the data by either classifying it into designed categories or else through the process of regression, which is an analysis of the relationship present among the studied variables of the model. Alternatively, unsupervised learning manipulates unlabelled data. In this case, human intervention is not needed as the deep learning algorithm becomes responsible for discriminating the patterns of the data and, once again, the relationships between the variables. This is mostly executed through the clustering and the association of the data. As opposed to supervised learning, unsupervised learning tends to involve a more complex process to yield a desirable output.

A basic understanding of how deep learning works allows one to further understand why it is becoming a popular tool in X-ray imaging. Generally, the principal objective behind the use of deep learning is the reconstruction of high-quality images when limited data is available. Furthermore, this brief introduction clarifies how the ONIX algorithm works, a deep learning model that is used in this project to push the limits of traditional tomography. The ONIX algorithm was developed by Yuhe Zhang, a Ph.D. student at Lund University, working at the Division of Synchrotron Radiation Research.

2.4.2 ONIX - Optimized Neural Implicit X-ray imaging - from 3D to 4D

ONIX is a deep learning algorithm that can be used to obtain high-resolution 3D object reconstructions from only a limited set of sparse projections. ONIX is basically a reconstruction algorithm for XMPI. An important underlying principle that makes ONIX such a practical algorithm is that it incorporates the physical background of the X-ray interaction with matter. ONIX is based upon neural implicit 3D representation. This approach aims to go beyond the traditional discrete representation of objects and nature which can provide just a limited amount of information, and instead deal with continuous functions. These continuous space functions perform the modeling of 3D volumes at arbitrary resolutions.

In summary three main features of ONIX are, (i) adding the physics behind X-ray-matter interaction, with a focus on the phase and attenuation terms of the X-rays, (ii) the integration of a convolutional layer which is responsible for transferring knowledge across different instances and (iii) the formulation of a continuous functions.

I. ONIX and the Physics of X-rays The main equation which describes the interaction of X-rays and matter is Equation 2.5, the complex expression for the refractive index,

describing the way X-rays interact, with a high penetration power and a weak likelihood of interaction. The projection approximation can be implemented in such cases. The exit wave can be characterized by a variation of Eq. 2.6, expressed as follows:

$$\Psi_{z_{exit}} = \Psi_{z_0} exp\left(-ik\int_{z=z_0}^{z=z_{exit}}(\delta[x,y;z]-i\beta[x,y;z])dz\right) \tag{2.18}$$

Transmitted X-rays can be approximated by the outgoing wave that leaves the object. The role of the approximation is to maintain consistency between the 2D and 3D spatial domains, by transferring information between the 2D sinograms and the 3D reconstructions.

II. ONIX and 3D Unsupervised Learning ONIX is a 3D unsupervised learning algorithm, a definition previously explained. Fig 2.11 show how ONIX works. In order for the approximation of a 3D sample to take place, the parameters used in the algorithm need to be optimized. The "loss function" of the neural network, typically called a cost function, is minimized in order to attain optimization. In Fig 2.11, one can see that the algorithm is trained with four views $(c_1, ..., c_4)$. Three random views are then used to constrain the 3D volume, therefore referred to as constraints. These constraints, with the aid of one of the neural networks, the encoder (**E**), is encoded into a high dimensional space, otherwise known as the latent space. A coordinate transformation **G** for the views changes the 3D global coordinate system to a local coordinate system. The local coordinates are defined by, e.g., $\mathbf{y}_1 = \mathbf{G}_1(\mathbf{x})$. Within these coordinate systems, the 3D volume is parametrized in terms of (i) the distance between a point and detector plane along the direction of the X-rays responsible for the view and (ii) the coordinates at which that ray intersected the camera plane. Another neural network (**F**) is then used the constraints and prior information given to reconstruct the 3D object.

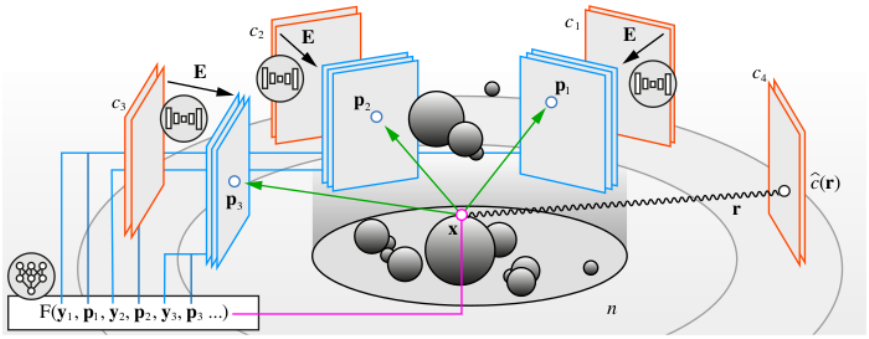

Figure 2.11: An illustration of how ONIX works. Here we have the four training views $(c_1, ..., c_4)$, where the first three are taken to be the constraints. The encoder **E** then encodes these constraints into latent space. (**F**) relates n (complex index of refraction) to the coordinates of the encoded views $(\mathbf{y_1}, \mathbf{y_2}, \mathbf{y_3})$ and their latent vectors $(\mathbf{p_1}, \mathbf{p_2}, \mathbf{p_3})$. Finally, the function between n (in 3D) and $\mathbf{x}$ (3D spatial coordinate) is learned by the algorithm through an optimization of the pixel value of c_4 and the predicted line integral of $n(\hat{c}(\mathbf{r}))$ along the ray $\mathbf{r}$. [29]

The main process taking place, in this case, is relating the index of refraction (**n**) to the local coordinates and their corresponding latent vectors $(\mathbf{p}_1, \mathbf{p}_2, \mathbf{p}_3)$ for the spatial coordinate of $\mathbf{x}$. Position encoding follows in the algorithm to map the spatial coordinates

to a higher dimensional space, from $\mathbb{R}$ to $\mathbb{R}^{\mathbb{L}}$. When the algorithm has gained enough 3D information about the refractive index $n(\mathbf{x})$, it becomes possible to calculate the 2D projection images at a desirable viewpoint. By optimizing the loss function:

$$\mathcal{L} = \sum_{\mathbf{r}\in R} ||c_V(\mathbf{r}) - \hat{c}(\mathbf{r})||_2^2 \tag{2.19}$$

where R is the collection of 2D rays and $\hat{c}$ stands for the estimated phase or attenuation contrast. The rays and projections are employed to train the parameters of the DL algorithm utilizing c_V, which are the measured views. The loss function is calculated over a selection of sampling points chosen. Pixel values for the phase and attenuation are computed with the following formula:

$$\hat{c} = \log(\Psi_z/\Psi_{z_0}) \sum_{j=1}^{N} \Delta_j(-ik\delta_j - k\beta_j) \tag{2.20}$$

where the distance between two neighbouring points is Δ_j. The difference between the pixel value of the $c_4(\mathbf{r})$ (the input image) and the line integral $\hat{c}(\mathbf{r})$ of n allows the algorithm to learn the function between the index of refraction n and the spatial coordinate $\mathbf{x}$. When using ONIX, a higher number of constraints used yields better and improved final reconstructions.

The discussion of ONIX here has been as a deep learning model in 3D. However, it has the capability to be used in 4D, which includes the fourth dimension of time. In this particular algorithm, the complex index of refraction would then become a function of both position and time. 4D-ONIX is a yet novel method, which if further implemented, would permit a better understanding of the dynamics of samples being studied, and have a decisive impact in fields like medicine or additive manufacturing.

The most important parameters associated with 4D ONIX (of which the first three are characteristic of all deep learning algorithms) are summarised below:

- **Batch size:** Number of objects trained in each epoch. Increasing the batch size might cause memory issues in the GPU, although the performance increases too. In this situation, a value between 2 and 3 was recommended.

- **Learning rate decay:** This is the decay factor of the learning rate, which causes the learning rate to decrease at given intervals. This decay is necessary to help the algorithm converge to the optimal value. [30]

- **Learning Rate:** This hyperparameter is important in helping determine the speed at which the network can update its learned concepts. It controls the weights (or learnable parameters) with respect to the loss gradient. [30]. A value too large may cause the network to overshoot and yield a decrease in the accuracy of the output.

- **Number of views:** These are the number of encoded projections that are used in each training iteration. The projections from the data correspond to the viewing angles of the 3D volume which has to be reconstructed. The default number of views is usually 4.

- **Number of epochs:** An epoch is defined as the moment when the all the training data has passed once through the algorithm. ONIX is usually trained with

around 300 - 400 epochs. Too low a number for the epochs results in underfitting of the data, while similarly increasing the epoch number can lead to overfitting, in both cases leading to bad reconstructions.

- **Lambda-GAN:** This is especially necessary when the algorithm is working with a small number of projections. GAN stands for Generative Adversarial Network and is a network that generates data in an attempt to fool the discriminator responsible for the classification of the true generated data and the "false" one [31]. High values of this imply that the generator will train to yield more realistic images (GAN loss given preference), and lower values will induce the generator to increase the accuracy of the reconstructions.

- **Lambda-MSE:** The weight for the MSE (Mean-Square Error) loss. High values of this parameter will exercise a minimization of the MSE between the ground truth and the actual reconstructed image, increasing the accuracy, whereas low values might prioritize other details at the expense of accuracy.

- **Training Error** It is the loss function that measures the differences between actual and predicted outputs of the model. It is given by the equation:

$$\text{Training Error} = \text{Total-MSE} + (\text{Lambda-GAN} \times \text{Generator loss}) \tag{2.21}$$

where the generator loss is simply the summation of the reconstruction losses at the coarse and fine levels. This latter part refers to how the algorithm reconstructs the images first in a general, coarse way with few details only to be then updated with all the necessary features, with a fine resolution.

3 METHOD AND TOOLS

3.1 PART I - TRADITIONAL TOMOGRAPHIC RECONSTRUCTIONS

For the study of the state-of-the-art tomographic reconstruction algorithms, two already obtained tomographic datasets from the TOMCAT beamline at the Paul Scherrer Institute (PSI) in Switzerland were used. The data had the following important parameters which had to be taken into consideration when carrying out the analysis:

Angular range [deg]	180
Number of projections	200
Number of X Pixels	1056
Number of Y Pixels	160
Number of sinograms	160
Number of angular positions	200

Table 3.1: Known data from the synchrotron X-ray tomography beamtime at PSI, per tomogram.

In total there were 800 tomograms with 160,000 projections for the first dataset (the reconstruction of the letters PSI) and for the second dataset (the reconstruction of a line), there were 500 tomograms with a total of 100,000 projections. The traditional tomographic reconstructions were carried out using TomoPy, which is a Python-based open-source software employed for the purpose of tomographic reconstruction and image processing. Thus, Gridrec and SIRT were studied using TomoPy as a function of the number of projections. Given the fact 200 projections were recorded for every 0 - 180 degrees rotation, there were 800 time-frames to be studied from the total number of projections as stated in Table 3.1. For the objective of carrying out the analysis between the two algorithms and the varying parameters, a frame was selected where the printing process has been completed. A proper slice for the visualisation of the reconstruction was also selected. By doing so, the letters "P","S","I" are expected to be seen. One of the features of TomoPy that was employed was the implementation of flat field correction (2.17). Similarly, for the center of rotation, a determining factor, which would greatly affect the quality of the reconstructed image if not chosen correctly, the TomoPy algorithm was run so that it would automatically determine the center of rotation, with 525.298 as the resultant value. This is a necessary step for synchrotron X-ray tomography where both the X-ray beam and the detector are kept at a fixed position and it is the sample that is rotated. [32]. The reconstruction is given the parameters of the number of projections, the angular range alongside the angular positions, the type of algorithm (such as Gridrec or SIRT), and in the case of SIRT, the number of iterations. The TOMCAT experiments were carried out in parallel beam geometry which simplifies the algorithm. Starting from 200 projections for a 180 angular range, the number of projections was gradually decreased.

An evaluation of the final image quality and the performance of these two algorithms was realized by calculating the SNR (signal-to-noise ratio), the CNR (contrast-to-noise ratio) of the collected reconstructions, and the computational time. The SNR and CNR were computed for a very specific reason: a general comparison of the qualities of the reconstruction outputs of the two algorithms. Likewise, close attention was paid to help determine the number of iterations in order to run the SIRT algorithm.

This is because the number of iterations is a crucial factor that conditions the quality of the final images. Usually, increasing the number of iterations considerably reduces noise [33]. However, too many iterations may also lead to the over-fitting of the data, resulting in reconstructions that lack accuracy.

The SNR is defined as the measure of the signal level of the reconstruction image to its background noise levels [34] and it is calculated by solving the equation:

$$\text{SNR} = \frac{\text{Signal Level}}{\text{Noise Level}} = \frac{\mu}{\sigma} \tag{3.1}$$

where μ is the mean signal and σ stands for the standard deviation. The SNR values were found using Python and were calculated for the whole reconstructed data, rather than just for one slice.

CNR is a ratio employed to assess the contrast existing between a chosen region of interest (ROI) in the reconstruction and its background [35]. To select the ROIs for the measurement of the CNRs, and get the necessary values required for the calculation of the ratio, ImageJ was employed. ImageJ is a software that permits the analysis of image data. The ROIs were then selected with the tool within ImageJ specifically designed for the purpose.

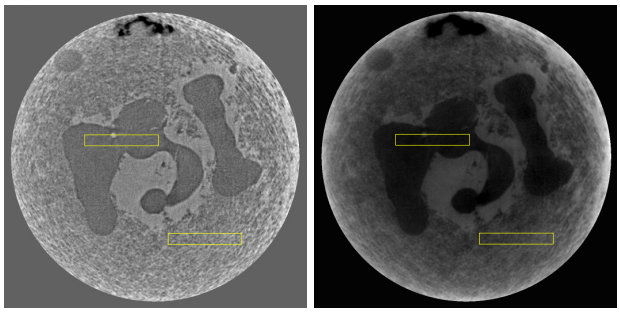

Figure 3.1: SIRT reconstructions of the 70th slice for 200 iterations and 25 iterations using 200 projections. The two main selected ROIs appear in both of the figures.

As Fig. 3.1 indicates, the main region of interest was the PSI letters themselves, in a way that the focus would be on how well one can discern them throughout all the reconstructions carried out. The background ROI was then also chosen, and its location is depicted in Fig. 3.1. The CNR is then measured by retrieving the intensity values, and their standard deviations using ImageJ, and is given by the formula:

$$\text{CNR} = \frac{|I_1 - I_2|}{\sqrt{\sigma_1^2 + \sigma_2^2}} \tag{3.2}$$

where the absolute contrast for the two ROIs I_1 and I_2 is $|I_1 - I_2|$ and the denominator represents the total noise, as σ_1^2 and σ_2^2 are the noise corresponding to each ROI. The calculations are made with Python and the results are presented in a table in Section 4.

In Section 2.3.2, the filtered backprojection algorithm was discussed, and it was mentioned how this process was improved through a regridding operation, with the new algorithm being denominated as Gridrec. The necessity of performing this step can be seen in Fig 3.2 below:

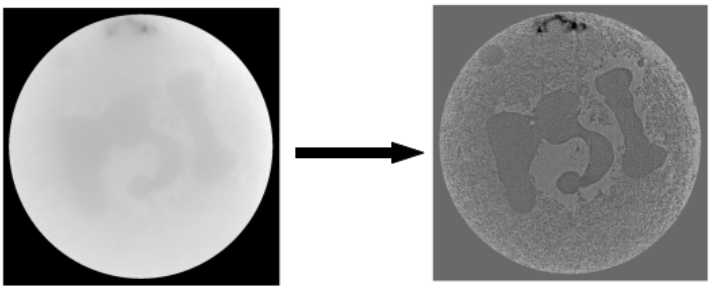

Figure 3.2: Reconstruction made with filtered backprojection (on the left) and Gridrec (on the right).

However, one of the problems with the Gridrec reconstructions is the noise in the final output. Therefore, post-processing has to be carried out on the reconstruction. Denoising of the reconstructed data was undertaken. The denoising method of median filtering was implemented with Python. This method is effective for the removal of impulse noise as it achieves this by modifying the pixel values in the data with the calculated median values of its neighboring pixels [36]. The last step was then to make the comparisons between the two algorithms and assess their performance when the number of projections gradually decreased.

3.2 PART II - RECONSTRUCTIONS WITH ONIX

This encompasses the second part of the thesis project, with the aim of obtaining a reconstruction using a limited number of projections. So, instead of using 200 projections, to begin with, as was the case with state-of-the-art algorithms like gridrec and SIRT, ONIX was made to run using only a file with 10 projections, spread out across the 180 degrees angular range. The dataset file was extracted with Python, in order to have a dataset that contained 10 projections with dimensions of 256x256 pixels. This time the tomographic data used was different, although acquired as well from TOMCAT beamline, this one included the projections of the attempt made at reconstructing a line. Of the 10 projections, only 8 projections were chosen for the training of the ONIX algorithm, while the remaining two projections served as validation views. The 8 projections for the training are employed in order to minimize the ground truth 3D model with the predicted 3D volume. The ground truth refers to the actual output the algorithm is trying to simulate. The two validation views are used by the same algorithm for the determination of the performance of ONIX, of how effectively the model generalizes to yet-to-be-observed data. The main parameters that need to be taken into consideration for the training are outlined in 2.4.2

Trainings of ONIX were performed on PyTorch 1.8.1 and Python 3.8.8 using an NVIDIA A100 GPU with 80 GB of RAM. 4 training attempts were made, each time changing some of the parameters described above. The first three training attempts kept a constant epoch number of 400, while for the final training experiment, the model was allowed to run for 500 epochs. In Section 7 (Appendix), a table showing the various parameters that differentiated the four training attempts has been included. Below, only the results for the best training attempt are shown.

Batch size	2
Learning rate	0.0001
Number of views	4 [1,3,5,7]
Epochs	400
Decay	0.9
Lambda GAN	1
Lambda MSE	5
Best training loss	1.102

Table 3.2: Training Attempt 1

The best training loss has been taken to be the lowest training loss attained by the algorithm, that indicates when the algorithm has learned the most and can approximate a high performance. It was calculated on Python using the generated values from the algorithm and using Eq. 2.21. While the training was happening, it was possible to supervise the performance of the algorithm by comparing the ground truth for the view angle for the validation with the resultant output after each epoch. An example of this is shown in Fig. 3.3. After the end of the training period, the final reconstructions were generated and visualized using SilxView, a software for image processing. From the results, one of the training attempts was chosen as the most successful and used for comparison with the traditional reconstruction algorithms. 3D rendering was carried out, with SilxView too, of the best training epoch of ONIX, and compared with the ground truth view.

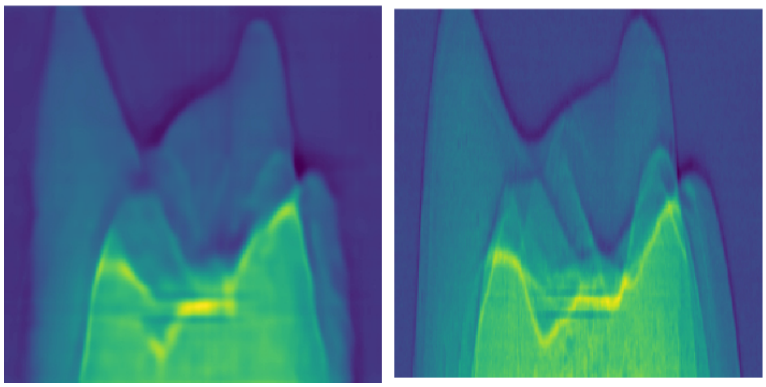

Figure 3.3: On the right of this figure is the ground truth, while on the right is the coarse figure obtained with the algorithm after running *Training Attempt 1* after 190 epochs.

4 Results & Discussion

4.1 PART I - SIRT vs GRIDREC

4.1.1 Studying the performance of state-of-the-art tomographic algorithms under the constraint of a limited number of projections

As the title of this subheading indicates and has been outlined in the methodology section, one of the main components of the thesis work was analyzing the performance of the two chosen state-of-the-art algorithms for tomographic reconstruction when their input data is decreased. This is one of their limitations, which is explained in 2.3.3, and one of the reasons why deep learning needs to be implemented for reconstructions with a sparse number of projections.

Before this study was dealt with, working with SIRT involved paying close attention to one of the features of the algorithm, the number of iterations that are meant to be used. In Fig. 4.1, the results are displayed when the SIRT algorithm was applied with a progressively reduced number of iterations for 200 projections. From 50 iterations, the image became gradually darkened, which makes it harder to distinguish the necessary details. Because the goal of this section was to lower the number of projections to a value at which both algorithms fail, it was decided to maintain the convention of having the number of iterations equal the number of projections for the SIRT algorithm. Thus at 200 projections, 200 iterations were run, and at 10 projections, the iterations were likewise lowered to 10. Linking both the projections and the iterations in this way implied that all the projection data was incorporated into the overall reconstruction process.

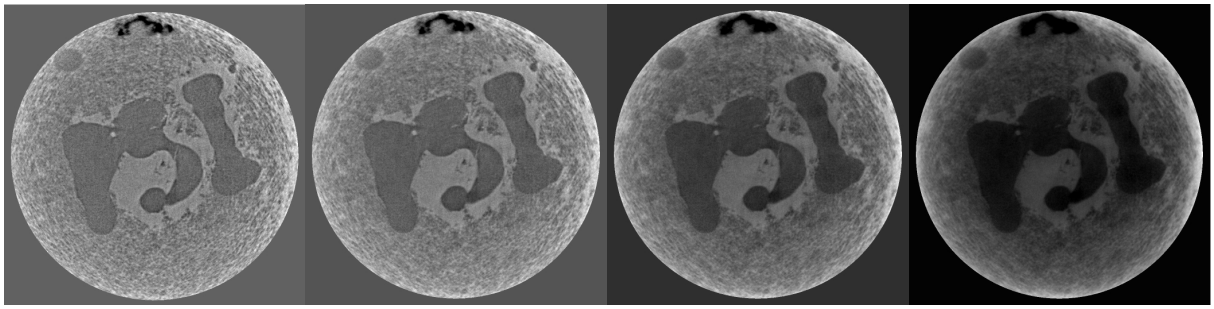

Figure 4.1: SIRT algorithm with 200, 100, 50, and 25 iterations (left to right). Each of these figures corresponds to the 70th slice of the reconstruction

In order to proceed with this study, image analysis was carried out. The importance of this step lay in obtaining two reconstructions when the highest number of available projections (200 projections in this case) was used that would allow a fair comparison between Gridrec and SIRT, in terms of image quality. For this reason, both the SNR and the CNR were computed for the reconstructions obtained for Gridrec and SIRT with 200 projections (a complete tomogram). Higher values for these ratios are synonymous with better image quality and resolution. The SNR for the SIRT algorithm yielded a value of 0.72, while for Gridrec, it was 0.32. This low value for the SNR indicated reconstructions with higher-than-needed salt-and-pepper noise, which decreased the overall image quality, as can be seen from Fig. 4.2. Following the implementation of median filtering to reduce the noise, the SNR was increased to 0.56.

From the resulting figure on the right of Fig. 4.2, which shows the reconstructed slice after denoising, and the first figure of Fig. 4.1 for the SIRT algorithm, the letters P-S-I can be clearly visualized in both cases and for the general purpose of the thesis, the qualities of the two reconstructions permitted a satisfactory comparison. In a similar fashion, the CNR values were computed and the same observations were noticed. For the SIRT reconstruction, a value of 1.13 was obtained for the CNR, and for Gridrec, the Contrast-to-Noise ratio was also increased through the removal of impulse noise, jumping from 0.29 to 0.80.

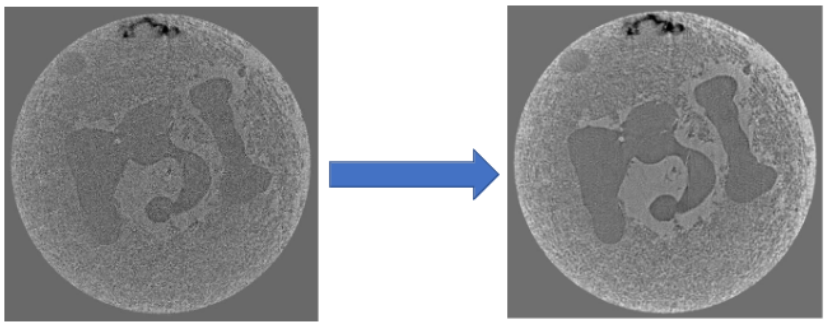

Figure 4.2: Gridrec algorithm before and after denoising. The letter "PSI" in the denoised figure at the right now appears more clearly upon the slice.

With all this considered, the resulting reconstructions were obtained for both SIRT and Gridrec, when the number of projections was lowered, from 200 projections, to 100 projections, 25 projections, and 10 projections respectively. Slices from these reconstructions are visualized in Fig. 4.3, for Gridrec, and in Fig. 4.4 for SIRT.

At 200 projections, the reconstructions from the two implemented algorithms can be regarded as analogous. These reconstructions are, in fact, what would be expected when performing the tomographies, where 200 projections are acquired when rotating the sample through a 180 degrees range. When the algorithms can process all available information from the data collected, the reconstructions are of suitable and high resolution. And while the reconstruction obtained with SIRT has a higher SNR, which means it has better quality, the downside of using this algorithm lies in the computational time it takes to achieve the reconstructions, as opposed to Gridrec, which yields good quality reconstructions, usually, after a matter of seconds. To be more precise, Gridrec took 51.91 seconds, as opposed to 79.3 minutes for the SIRT algorithm. This is something to be expected for the SIRT algorithm because as was demonstrated in Section 2.3.2, there are different factors that result in the slow processing, such as the iterations involved in the reconstruction and the matrix operations, which when dealing with large datasets, are computationally intensive. At this stage, when a complete dataset is used, Gridrec is the algorithm most widely used in the field of tomographic reconstruction due to its fast results, and with the necessary image processing techniques, high-quality images can be produced. However, the picture changes when the number of projections is decreased.

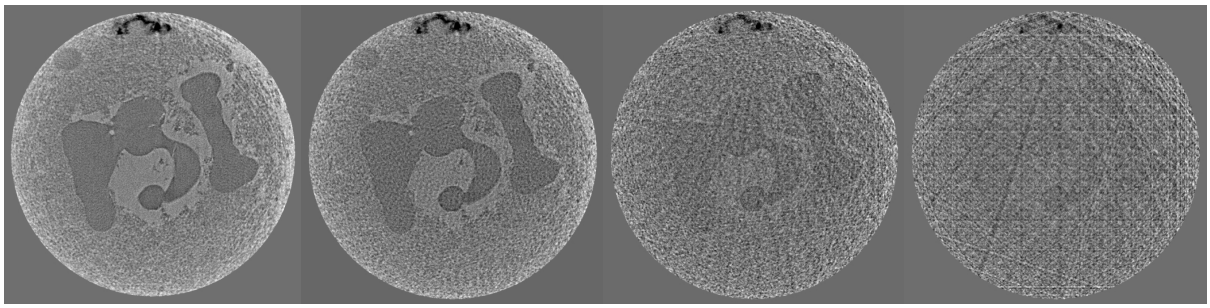

(a) 200 projections **(b)** 100 projections **(c)** 25 projections **(d)** 10 projections

Figure 4.3: Gridrec tomographic reconstructions for a decreasing number of projections.

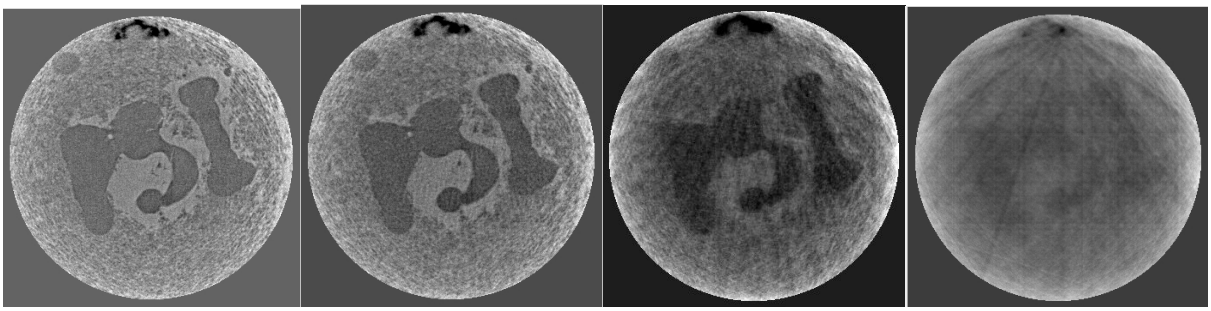

(a) 200 projections **(b)** 100 projections **(c)** 25 projections **(d)** 10 projections

Figure 4.4: SIRT tomographic reconstructions for a decreasing number of projections.

As we reach 100 projections, the GRIDREC algorithm begins to show a considerably higher amount of noise as opposed to the reconstruction using the SIRT algorithm, which still preserves its high level of quality. And at 25 projections, the noise amplification is very clearly evident. A type of artifact, known as *aliasing* can be likewise observed in parts c) and d) of Figure 4.3. These refer, for clarification, to the fine lines that appear to be crossing the slice, originating from the object. Aliasing artifacts are a direct result of under-sampling. When only 10 projections are employed, it can unmistakably be stated that the algorithm has failed, as the reconstruction obtained bears no resemblance to the original object (Figure (a)), and no usable analysis can be attained from it. Using Gridrec with only a few projections available is simply not an option. Gridrec is an algorithm that is highly dependent on having a large angular coverage of projections. This relates back to the concept of Crowther's criterion, which has to be followed for the precise representation of the object's frequency contents (refers to the variation in the intensity or density of the studied sample). Given that each projection contains information about the spatial distribution of the object, a decrease in the number of projections means that there is not enough information on which to reconstruct the image, and necessary spatial features will be missing.

In the case of the reconstructions the SIRT algorithm yields, and when comparing them to the ones obtained with Gridrec, it can be concluded that this algorithm is able to work more efficiently when there are limited projections. At 25 projections, although aliasing artifacts emerge, the letters P-S-I remain visible, unlike the case for Gridrec, where the noise greatly diminishes the ability to distinguish the important detail of the letters. At 10 projections, the letters have become extremely blurry and it

is hard to differentiate these from the background, and it would not be feasible to do any further analysis on the resulting reconstructions. So, in this situation, two statements can be made. SIRT is still the better-performing algorithm of the two. Leaving behind the computational time, SIRT produces high-quality images, which are not affected by increased levels of noise, and which can still be easily used when the number of projections is reduced. The principal reason for this optimized performance is the iterative nature of SIRT. The iterations involved in this algorithm allow the gradual refinement of the reconstruction after a number of iterations, as the process involves updating the image at each step using all the available projection data, and by using the convention outlined before between the number of projections and the number of iterations, further aids with this. The second statement involves arguing the case that despite SIRT being the best algorithm of the two studied in this section, it also fails when we reach 10 projections, and thus using this number or even decreasing it will not give viable results.

On the basis of the results obtained, it can then be affirmed that achieving a tomographic reconstruction for sparse projections/data is not possible using the traditional reconstruction algorithms and other new methods need to be employed to overcome this limitation. To achieve results when reducing the constraints in terms of the number of projections, the novel deep learning algorithm of ONIX needs to be employed.

4.2 PART II - Image reconstruction with ONIX

4.2.1 Studying the performance of the XMPI deep learning algorithm, ONIX, with a limited number of projections, and comparing it with the results obtained for SIRT and Gridrec under the same constraint.

Given the fact that the traditional reconstruction algorithms produced undesirable results for a limited number of projections, ONIX, the deep learning algorithm for XMPI, was implemented. As was outlined in the Methods Section (Section 3), the second dataset (reconstruction of a line) was used to train the ONIX algorithm. And for the remaining part of the thesis work, this specific dataset was used, and all the procedures performed on the first dataset (the reconstruction of the letters P-S-I), which are illustrated in Section 3 and in Part I of Section 4.1 are once again carried out on the second dataset, namely, to obtain the reconstructions using SIRT and Gridrec when the number of projections is decreased and using these for comparison purposes against the output of the ONIX algorithm.

The ONIX algorithm was trained with 8 projections only, and with these 8 projections, ONIX was capable of rendering the reconstruction of the studied dataset. Various training attempts were made in order to see which would yield the best results that were aimed for in this section. In Fig 4.5, results for the best training, Training Attempt 1, are shown. In this case, these are not the reconstructions, but rather what is seen here is the captured information that is observed from a given perspective, representing the information carried by each projection. In the figure, this is the ground truth corresponding to one of the views, or projections used. Based on this, ONIX is responsible for creating a coarse output. This coarse output is the obtained prediction of the

object's properties as the algorithm tried to learn from the available projections. After each epoch, when the loss function is optimized and the parameters adjusted, ONIX gradually improves the quality of the coarse output to make it resemble the ground truth. The better the coarse output resembled the ground truth, the better the reconstruction was going to be. Fig. 4.5 shows the coarse outputs obtained after training for 190, 200, and 300 epochs. The coarse output for Epoch 190 turned out to be the one most similar to the ground truth, and when the training loss was calculated for these three results, its value of 1.102 turned out to be the lowest, thus confirming that it corresponded to the best reconstruction. This is because a lower training loss meant the algorithm had been able to strongly learn the patterns and structures of the training data. It is to be supposed that above 200 epochs, the model starts to be over-trained, and the quality begins to deteriorate.

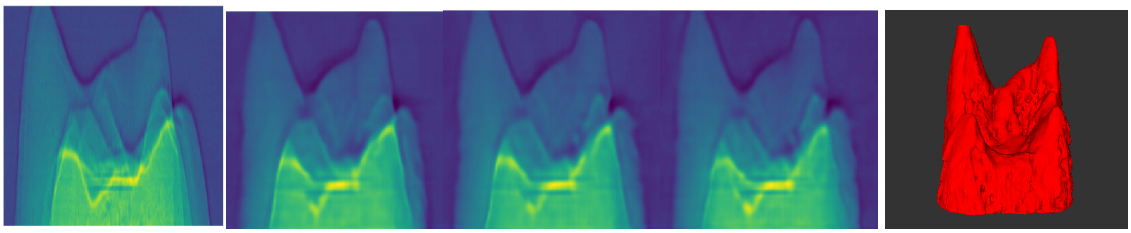

(a) Ground truth **(b)** 190 epochs **(c)** 200 epochs **(d)** 300 epochs **(e)** 3D - Epoch 190

Figure 4.5: Coarse output figures and final 3D rendering for **Training Attempt 1**

Training ONIX proved to be the most challenging aspect of the thesis work, and that is why four main training attempts were made, in order to increase the likelihood of securing a good reconstruction. General results for the other training attempts have been included in the Appendix, in Section 7. Comparing Table 3.2 with Tables 7.2 - 7.4 (Appendix) offer an indication as to why two of the training attempts did not succeed. Technically, it seems that the learning rate played the greatest factor, as the two where it was increased from 0.0001 to 0.0002 showed the worst coarse outputs. The implication was that increasing the value led to unstable training, and was not satisfactory for the architecture of this problem. Furthermore, a grave mistake was even attempting to do a training with a Lambda GAN value set to 0, as completely neglecting the adversarial loss will undoubtedly lead to distorted results, with poor quality. Although it would have been possible to continue adjusting parameters to try and achieve an even better reconstruction, given the period of time for this project, Training Attempt 1 was suitable for the purpose of proving how, by using a deep learning algorithm, it is possible to overcome one of the limitations found for the state-of-the-art reconstruction algorithms, as it can work with a sparse number of views.

The final reconstructions with ONIX, achieved with only 8 projections, are presented in Fig. 4.6, for the training made at 190, 200, 300, and 400 epochs. These results are compared with the reconstructions obtained with both Gridrec and SIRT. Once again, Fig. 4.7 and Fig. 4.8, convey one of the slices from the reconstructions obtained for the second dataset, at 200 projections, followed by how it changes as the number of projections is lowered. This time, instead of remaining at 10 projections, the number is lowered to 8 projections, which is the point at which the ONIX algorithm was made to train and can be used for comparison. The result for 200 projections for both SIRT and Gridrec is the expected outcome, the target object of the tomographic

investigation. And as was examined in close detail in Part I (4.1) of the Results section, the lower the input data for these two algorithms, the worst the reconstruction will be, and at 8 projections, it can be witnessed from the figures that both have failed, confirming one more time why ONIX is a requirement if one aims to achieve image reconstructions when the input data is critically limited. In fact, Fig. 4.7 and Fig. 4.8 basically present the same results that appear in Figures 4.3 and 4.4, although this time the second dataset is employed.

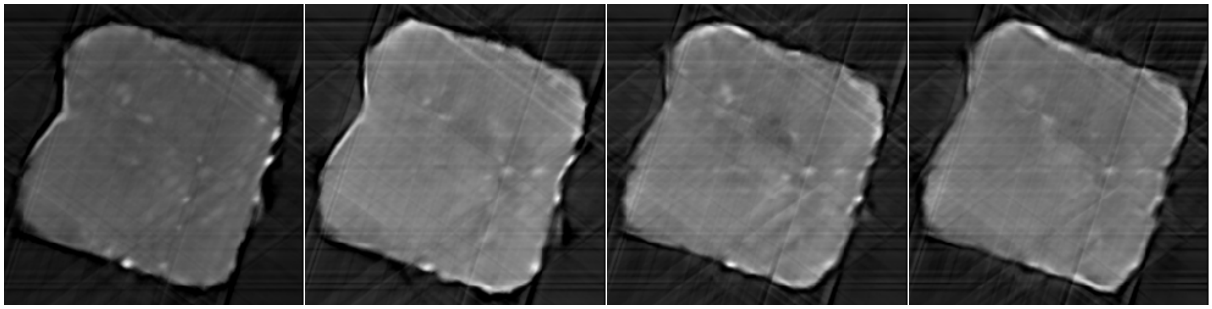

(a) T1 - Epoch 190 **(b)** T1 - Epoch 200 **(c)** T1 - Epoch 300 **(d)** T1 - Epoch 400

Figure 4.6: Reconstructions with ONIX for an increasing number of epochs.

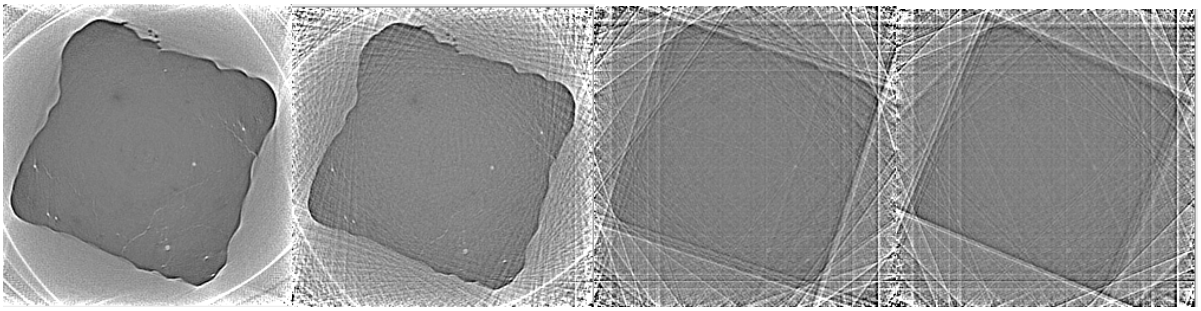

(a) 200 projections **(b)** 50 projections **(c)** 10 projections **(d)** 8 projections

Figure 4.7: Gridrec tomographic reconstructions for a decreasing number of projections.

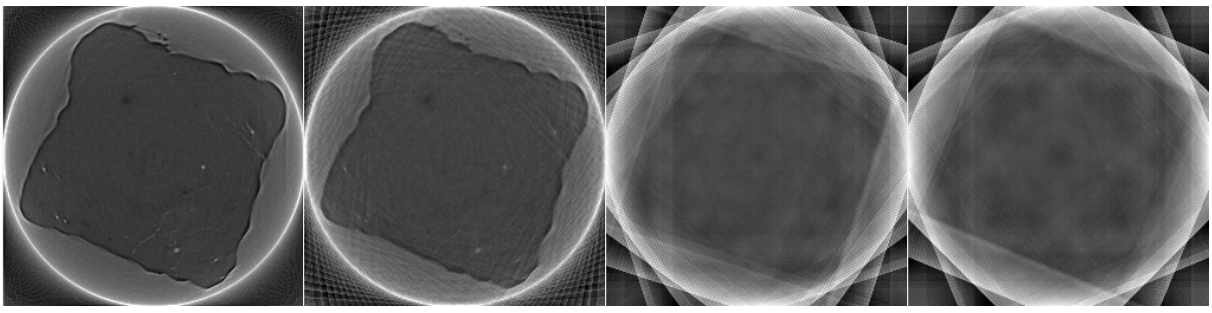

(a) 200 projections **(b)** 50 projections **(c)** 10 projections **(d)** 8 projections

Figure 4.8: SIRT tomographic reconstructions for a decreasing number of projections.

The results for ONIX (Fig. 4.6) confirm and establish the aim of this project. The reconstructions are, indeed, what was expected. The shape that was traced out during

tomographic acquisition and now viewed in the reconstructions for SIRT and Gridrec with 200 projections is the same that now appears in the reconstructed slices attained with ONIX. The images for a different number of epochs are exhibited in Fig. 4.6 but this is mainly done to give the general picture of the results achieved with the deep learning algorithm. Even when it was settled that the reconstruction after 190 epochs was the best due to having the lowest training error, the final reconstructions for epochs 200, 300, and 400 are still comparable to it, and the four figures represent the reconstruction shape that had to be and was achieved.

A clear conclusion can be derived from this, ONIX, thanks to its architecture, has been able to encode the information from the eight projections it was trained with, and use these eight projections to carry out a complete reconstruction. This is the same result one can expect to retrieve when using a full set of projections with the Gridrec and SIRT algorithms. Despite having discussed that SIRT performs better than Gridrec when the projections are decreased, it is also not suitable when seeking a reconstruction with only a very limited number of projections. X-ray multi-projection imaging and deep learning, however, overcome this constraint and support 3D reconstructions when a sparse number of views are utilized. This capability of ONIX, which has here been duly demonstrated, can prove groundbreaking if used in fields like additive manufacturing (3D printing).

5 Outlook

5.1 ONIX and Additive Manufacturing

One of the most common uses of tomography and X-ray imaging is additive manufacturing. Additive manufacturing refers to the process of creating 3D objects through the process of progressively adding layer upon layer of material until the desirable 3D structure is reached. One of the most common techniques is known as *Laser powder-bed fusion (L-PBF)*, widely employed by industries such as the aerospace industry, and which can be used for the creation of complex materials. Its working principle involves repeatedly melting a thin layer of powder until the 3D object is built. [37]. Incorporating X-ray imaging techniques is a promising way of further developing the field of additive manufacturing. This is because X-ray imaging is a mechanism that allows the study of the dynamics of materials being produced through this process. That is, a close analysis of the behavior of the materials as it is being printed, with a focus on the changes affecting them. The dynamics of physical systems are thus an important and continuous source of study within additive manufacturing. Synchrotron X-rays have become a tool that has the distinct advantage of being able to pursue the analysis of "real materials under real conditions in real time" [38]. This is precisely why further studies and new developments in the area of X-ray imaging are imperative for the progress of additive manufacturing. Emerging tools through which to incorporate fast dynamics, that can save both time and money and still likewise provide high-resolution outputs for real-time study of the materials is an aspect of this research. A deep learning algorithm like ONIX has enormous possibilities and potential to be used in additive manufacturing. Although still a novel method, even during the scope of this bachelor's project, it has been made possible to carry out a 3D reconstruction with an astonishing limited range of projections (input data). Further studies with ONIX can be groundbreaking in improving the introduction of 3D dynamics in additive manufacturing studies, for reasons sketched in Section 1.

6 Conclusion

The aim of this bachelor's thesis was to become familiar with the state-of-the-art reconstruction algorithms used in synchrotron X-ray tomography, and then explore the capabilities of ONIX, a new deep-learning algorithm developed at Lund University, for the purpose of tomographic reconstruction.

The project was, for the most part, computational, paying particular attention to a qualitative comparison between the reconstructed outputs produced by the three principal algorithms used, Gridrec, which is a preferred option in modern-day X-ray tomography due to its fast processing capability, and 3D images that can very well be studied and analyzed, then SIRT, an iterative and superior method for reconstructions and finally ONIX, the deep learning approach. After undertaking some quantitative analysis of the reconstructions to establish their quality, the work focused mostly on pushing the limits of traditional tomography. Exploring one of the disadvantages of these algorithms, which is how they cannot handle a limited amount of data, and this was done by gradually decreasing the number of projections for the reconstruction, confirming the fact that the image quality plummeted and both Gridrec and SIRT failed when they had to process only 10 projections. This highlighted the importance of hav-

ing another algorithm that could overcome this limitation, and this is why ONIX was implemented, a deep learning algorithm for XMPI, which by incorporating a physics-based loss function, and the integration of prior knowledge about the imaging process, results in better reconstructions, even with a sparse number of projections. Reconstruction was successfully achieved with ONIX, and the results obtained were compared to the ones from the traditional algorithms. Using two different datasets to conduct the two main components of this thesis, created a more versatile form of studying the implications of X-ray tomography, and the indispensability of new methods like ONIX, whose implication in fields like additive manufacturing can prove crucial, in the acquisition of knowledge of the dynamics of materials being created.

The possibilities of ONIX have barely been exploited, and it is to be expected that in the future it will become a usual tool in X-ray imaging. The number of projections integrated into the algorithm can be further diminished, and it is expected to even work with as low as two projections. Therefore, its use could well extend beyond additive manufacturing, with potential applications in the medical and biological fields.

REFERENCES

[1] J. Als-Nielsen and D. McMorrow. "Elements of Modern X-ray Physics". In: John Wiley & Sons, Ltd, 2011. Chap. Chapter 9: Imaging, pp. 305–342. URL: https://onlinelibrary.wiley.com/doi/10.1002/9781119998365.ch9.

[2] J. Als-Nielsen and D. McMorrow. "Elements of Modern X-ray Physics". In: John Wiley & Sons, Ltd, 2011. Chap. Chapter 1: X-rays and their interaction with matter, pp. 1–28. URL: https://onlinelibrary.wiley.com/doi/abs/10.1002/9781119998365.ch1.

[3] National Institute of Standards and Technology. *Kilogram, Mass, and Planck's Constant*. URL: https://www.nist.gov/si-redefinition/kilogram-mass-and-plancks-constant (visited on 04/20/2023).

[4] Physics LibreTexts. *The Electromagnetic Spectrum*. URL: https://phys.libretexts.org/Bookshelves/University_Physics/Book%3A_Physics_(Boundless)/23%3A_Electromagnetic_Waves/23.1%3A_The_Electromagnetic_Spectrum (visited on 02/15/2023).

[5] D. M. Paganin. "X-ray interactions with matter". In: *Coherent X-Ray Optics*. Oxford University Press, 2006, pp. 397–405. URL: https://doi.org/10.1093/acprof:oso/9780198567288.003.0002.

[6] P. Willmott. "An Introduction to Synchrotron Radiation". In: John Wiley & Sons, Ltd, 2011. Chap. Imaging Techniques, pp. 303–337. URL: https://onlinelibrary.wiley.com/doi/abs/10.1002/9781119970958.ch7.

[7] Radiation Dosimetry. *What is Photoelectric Absorption of X-rays? Definition*. URL: https://www.radiation-dosimetry.org/what-is-photoelectric-absorption-of-x-rays-definition/ (visited on 02/28/2023).

[8] B. Nett. *X-Ray Interactions*. URL: https://howradiologyworks.com/x-ray-interactions/ (visited on 02/28/2023).

[9] ScienceDirect. *Compton Scattering*. URL: https://www.sciencedirect.com/topics/medicine-and-dentistry/compton-scattering (visited on 03/01/2023).

[10] J. T. et al Bushberg. "The Essentials of Medical Imaging 3rd ed." In: Lippincott Williams Wilkins, 2012. Chap. Interaction of Radiation with Matter, pp. 33–60.

[11] M. Bertolo et al. "X-ray Spectromicroscopy with Synchrotron Radiation: Approaches and Applications". In: (2017). URL: https://www.researchgate.net/publication/237593105_X-ray_Spectromicroscopy_with_Synchrotron_Radiation_Approaches_and_Applications (visited on 04/12/2023).

[12] C. Jacobsen. "X-Ray Tomography". In: Advances in Microscopy and Microanalysis. Cambridge University Press, 2019. Chap. X-Ray Microscope Instrumentation, pp. 321–349.

[13] Y. Wenbing et al. "Next-generation high-brightness x-ray sources with tunable x-ray spectrum (Conference Presentation)". In: *Advances in Laboratory-based X-Ray Sources, Optics, and Applications VII*. Ed. by A. Murokh and D. Spiga. Vol. 11110. International Society for Optics and Photonics. SPIE, 2019, p. 111100D. URL: https://doi.org/10.1117/12.2530366.

[14] D. Bernard. *History of X-rays – 125 years in the making (pt 2)*. URL: https://www.excillum.com/history-of-x-rays-x-ray-tubes/ (visited on 04/18/2023).

[15] R. Aamir. *Using MARS Spectral CT for Identifying Biomedical Nanoparticles*. ResearchGate. Aug. 2013. URL: https://www.researchgate.net/publication/257029228_Using_MARS_Spectral_CT_for_Identifying_Biomedical_Nanoparticles.

[16] P. Willmott. "An Introduction to Synchrotron Radiation". In: John Wiley Sons, Ltd, 2011. Chap. Synchrotron Physics, pp. 39–86. URL: https://onlinelibrary.wiley.com/doi/10.1002/9781119970958.ch3 (visited on 04/15/2023).

[17] K. Bourzac. *This X-ray laser is getting faster and brighter*. URL: https://cen.acs.org/physical-chemistry/X-ray-laser-getting-faster/100/i26 (visited on 04/18/2023).

[18] National Cancer Institute. *Radiation Therapy*. URL: https://www.cancer.gov/about-cancer/treatment/types/radiation-therapy (visited on 03/14/2023).

[19] C. Xu et al. "3D Visualized Characterization of Fracture Behavior of Structural Metals Using Synchrotron Radiation Computed Microtomography". In: *Quantum Beam Science* 3.5 (2019).

[20] T. Roelandts. *Tomography, Part 3: Reconstruction*. URL: https://tomroelandts.com/articles/tomography-part-3-reconstruction (visited on 04/03/2023).

[21] B. Vandeghinste. "Iterative Reconstruction in Micro-SPECT/CT: Regularized Sparse-View CT and Absolute In Vivo Multi-Isotope Micro-SPECT Quantification". PhD thesis. Ghent University, 2014. URL: https://www.ugent.be/ea/ibitech/en/about-us/medisip-staff/phd/dr_ir_bert_vandeghinste.pdf.

[22] Brabant, L. and Vlassenbroeck, J. and De Schryver, T. and Boone, M. and Van Hoorebeke, L. "The advantages of iterative reconstruction methods for high resolution X-ray tomography". In: *12th International conference on X-Ray Microscopy : conference program handbook*. 2014, pp. 273–273. URL: https://biblio.ugent.be/publication/5778935 (visited on 02/27/2023).

[23] Wikipedia. *Algebraic Reconstruction Technique*. URL: https://en.wikipedia.org/wiki/Algebraic_reconstruction_technique (visited on 04/17/2023).

[24] V. Hart. "The Application of Tomographic Reconstruction Techniques to Ill- Conditioned Inverse Problems in Atmospheric Science and Biomedical Imaging". PhD thesis. Utah State University, 2012. URL: https://digitalcommons.usu.edu/etd/1354 (visited on 04/20/2023).

[25] R. Aprilliyani, R. G. Prabowo, and Basari. "On the performance of SART and ART algorithms for microwave imaging". In: *AIP Conference Proceedings* 1933.1 (Feb. 2018). URL: https://doi.org/10.1063/1.5023980 (visited on 03/15/2023).

[26] S. Vandenberghe, J. De Beenhouwer, and I. Lemahieu. "Iterative reconstruction algorithms in nuclear medicine". In: *Computerized medical imaging and graphics: the official journal of the Computerized Medical Imaging Society* 25.2 (2001), pp. 105–111.

[27] H. Zhou B.and Li, Xiaochuan Wang, and G. Wang. "Limited View Tomographic Reconstruction Using a Cascaded Residual Dense Spatial-Channel Attention Network With Projection Data Fidelity Layer". In: *IEEE transactions on medical imaging* 40.7 (2021), pp. 1792–1804.

[28] P. Villanueva-Perez et al. "Hard x-ray multi-projection imaging for single-shot approaches". In: *Optica* 5.12 (Dec. 2018), pp. 1521–1524. URL: https://opg.optica.org/optica/abstract.cfm?URI=optica-5-12-1521.

[29] Y. Zhang et al. "ONIX: an X-ray deep-learning tool for 3D reconstructions from sparse views". In: *Applied Research* (). DOI: https://doi.org/10.1002/appl.202300016. URL: https://onlinelibrary.wiley.com/doi/abs/10.1002/appl.202300016.

[30] You Kaichao et al. "How does learning rate decay help modern neural networks?" In: *CoRR* abs/1908.01878 (2019). URL: http://arxiv.org/abs/1908.01878 (visited on 04/21/2023).

[31] J. Rocca. *Understanding Generative Adversarial Networks (GANs)*. 2019. URL: https://towardsdatascience.com/understanding-generative-adversarial-networks-gans-cd6e4651a29 (visited on 04/10/2023).

[32] D. Gursoy et al. "TomoPy: a framework for the analysis of synchrotron tomographic data". In: *Journal of synchrotron radiation* 21.5 (2014), pp. 1188–1193. URL: https://www.ncbi.nlm.nih.gov/pmc/articles/PMC4181643/ (visited on 04/25/2023).

[33] C. Anam et al. "An investigation of spatial resolution and noise in reconstructed CT images using iterative reconstruction (IR) and filtered back-projection (FBP)". In: *Journal of Physics: Conference Series* 1127.1 (Jan. 2019), pp. 12–16. URL: https://dx.doi.org/10.1088/1742-6596/1127/1/012016.

[34] M. Welvaert and Y. Rosseel. "On the definition of signal-to-noise ratio and contrast-to-noise ratio for FMRI data". In: *PloS one* 8.11 (2013). DOI: 10.1371/journal.pone.0077089.

[35] Shenzhen Uni X-ray Technology Limited. *Contrast to Noise Ratio: Definition and Importance*. https://www.unixray.com/contrast-to-noise-ratio/. (Visited on 05/01/2023).

[36] R. Fisher and K. Dawson-Howe. *Median filtering*. 2005. URL: https://homepages.inf.ed.ac.uk/rbf/HIPR2/median.htm (visited on 04/25/2023).

[37] P. Lhuissier et al. "In situ 3D X-ray microtomography of laser-based powder-bed fusion (L-PBF) - A feasibility study". In: *Additive Manufacturing* 36 (2020), p. 101271. URL: https://www.sciencedirect.com/science/article/pii/S2214860420306436?via%3Dihub (visited on 04/29/2023).

[38] T. Sun. "Operando systems for synchrotron studies of additive manufacturing processes". In: *Review of Scientific Instruments* 93.11 (Nov. 2022). URL: https://doi.org/10.1063/5.0131804 (visited on 04/29/2023).

7 APPENDIX

TRAINING ATTEMPTS WITH ONIX

Batch size	2
Learning rate	0.0001
Number of views	4 [1,3,5,7]
Epochs	400
Decay	0.9
Lambda GAN	1
Lambda MSE	5
Best training loss	1.102

Table 7.1: Training Attempt 1

Batch size	3
Learning rate	0.0002
Number of views	4 [1,3,5,7]
Epochs	400
Decay	0.5
Lambda GAN	0
Lambda MSE	10

Table 7.2: Training Attempt 2

Batch size	2
Learning rate	0.0002
Number of views	6 [1,2,3,5,6,7]
Epochs	400
Decay	0.5
Lambda GAN	0.5
Lambda MSE	5

Table 7.3: Training Attempt 3

Batch size	2
Learning rate	0.0001
Number of views	4 [1,3,5,7]
Epochs	500
Decay	0.5
Lambda GAN	1
Lambda MSE	10

Table 7.4: Training Attempt 4

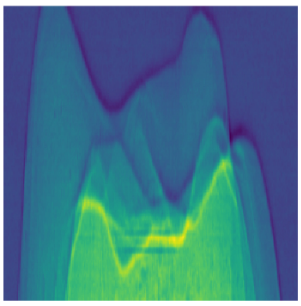

(a) Ground truth

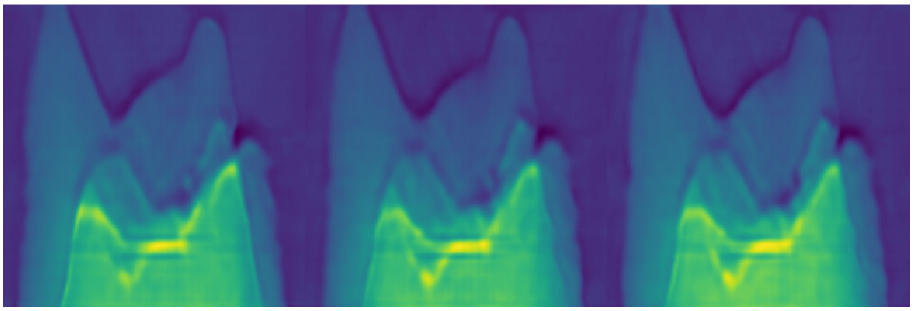

(b) 200 epochs **(c)** 300 epochs **(d)** 400 epochs

Figure 7.1: Coarse output figures for **Training Attempt 1**

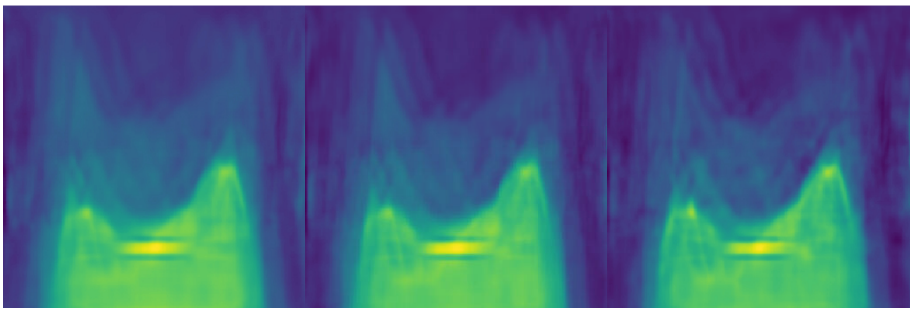

(a) 200 epochs **(b)** 300 epochs **(c)** 400 epochs

Figure 7.2: Coarse output figures for **Training Attempt 2**

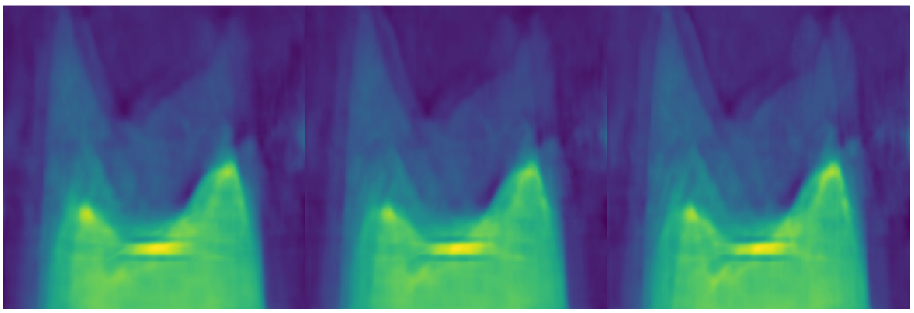

(a) 200 epochs **(b)** 300 epochs **(c)** 400 epochs

Figure 7.3: Coarse output figures for **Training Attempt 3**

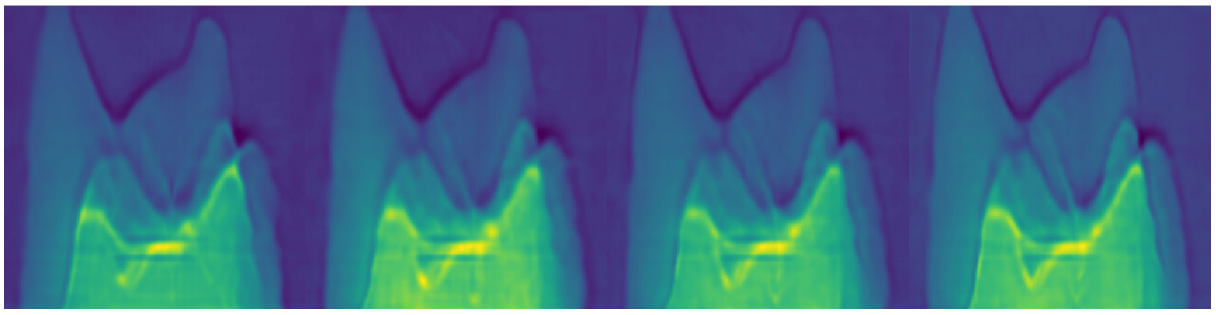

(a) 200 epochs **(b)** 300 epochs **(c)** 400 epochs **(d)** 500 epochs

Figure 7.4: Coarse output figures for **Training Attempt 4**